6-8-1999

Hardware-software integration for particle light scatter imaging

Christophe Pierre Godefroy
Florida International University

FLORIDA INTERNATIONAL UNIVERSITY

Miami, Florida

HARDWARE-SOFTWARE INTEGRATION FOR PARTICLE LIGHT SCATTER IMAGING

A thesis submitted in partial fulfillment of the

requirements for the degree of

MASTER OF SCIENCE

in

COMPUTER ENGINEERING

by

Christophe Pierre Godefroy

1999

To: Dean Gordon R. Hopkins
College of Engineering & Applied Sciences

This thesis, written by Christophe Pierre Godefroy, and entitled Hardware-Software Integration For Particle Light Scatter Imaging, having been approved in respect to style and intellectual content, is referred to you for judgment.

We have read this thesis and recommend that it be approved.

Dr. Jean Andrian

Dr. Armando Barreto

Malek Adjouadi, Major Professor

Date of Defense: June 8, 1999

The thesis of Christophe Pierre Godefroy is approved.

Dean Gordon R. Hopkins
College of Engineering & Applied Sciences

Dean Richard L. Campbell
Division of Graduate Studies

Florida International University, 1999

DEDICATION

To my parents, Alain and Monique Godefroy, and my brother, Hervé, who have always offered encouragement regardless of my choices. Thank you for being so patient and understanding.

ACKNOWLEDGMENT

I would like to express my heart-felt gratitude and appreciation to my thesis advisor, Dr. Malek Adjouadi, whose unselfish support and positive attitude always helped me through the rough times. His dedication and striving for perfection at his duties did not stop him in making his expertise available at any time of the day but also many nights as well!! Thank you again.

Many thanks to my committee members, Jean Andrian and Armando Barreto, who have take the time to help me in many occasions.

I could not have done this work without the constant moral and intellectual support of my best friend John Riley, and also the friendship and intellectual stimulation of co-workers like Jim Wyatt , Fuat Uler, Luis Garcia, Mark Wells, Chira Deka and Weijan Gong.

Last, but not least to my lovely wife, Maria Elena, to wish I express deep gratitude for her love, sacrifice, and encouragement throughout this long process. To my daughter, Elodie, and newborn son, Brandon, I love you both deeply.

ABSTRACT OF THE THESIS

HARDWARE-SOFTWARE INTEGRATION FOR PARTICLE LIGHT SCATTER IMAGING

by

Christophe Pierre Godefroy

Florida International University, 1999

Miami, Florida

Professor Malek Adjouadi, Major Professor

The main purpose of this research is the implementation of a software interface. This interface shall allow the interpretation of particle size in a medium with respect to its diffraction patterns. The literature shows extensive work on the theory of light scattering but the experiments are cumbersome to implement. Some initial work has required the levitation of particle to isolate the difficulties associated with a flow environment. The purpose of this work; however, will focus on the software requirements to synchronize, collect and analyze light scattering patterns.

Although there are many other ways of sizing particles, it may be useful to prove the feasibility of the well-defined theory in a flow environment.

The light scattering signatures from an illuminated particle is abundantly used in the flow cytometry area but are obtained from other mean in capturing light information. The present study could determine the specific angles of interest allowing the discrimination by size of various types of particles (e.g.. blood cells).

Table of Contents

LIST OF FIGURES

FIGURE PAGE

1 INTRODUCTION

1.1 Motivation of this Research Endeavor

The theory of scattering light of a non-absorbing spherical particle was first reported by L. Lorenz in 1890 and published by G. Mie in 1908. This theory is now known as the Lorenz-Mie Theory and sometimes simply referred as the Mie Theory. More recently, with the advancement of computer throughput, a growing interest in modeling scattering patterns of electromagnetic beam source by particles has emerged. Although this theory originates from the very beginning of this century, it's only in the last two decades that a particular effort has been devoted in not only efficiently describing the Lorenz-Mie theory but also the description of arbitrary shaped beams as the illuminating wave. The extension of Mie Theory, which is of a great interest in optical particle sizing, is scattering of a sphere by a laser beam having a Gaussian intensity distribution. The description of these laser beams has lead to the generalization of the theory [G. Gouesbet, 82] to take into account that the source can not be only considered as a pure plane wave.

Although a plethora of techniques for laser-based particle illumination exist, there are few experimental data to illustrate the theory. The literature search has revealed a few experiments with respect to light scattering signatures of particles in flow. Many experiments are geared towards levitated spherical droplets [J.T. Hodges,95].

1.2 Research Purpose

The focus of this thesis is on the software development of an interface that will prove the correlation between the expected scatter patterns of homogeneous particles and

its application to a particle sizer. The theoretical foundation of the Lorenz-Mie theory is hence related to a real world implementation using a special instrument with microscopic particles.

The purpose of this research is in the actual software development and its implementation to realize such an interface. This interface shall allow the interpretation of particle size in a medium with respect to its diffraction patterns. The literature shows extensive work on the theory of light scattering but the experiments have not related the theory to particles in flow. Some initial work has required the levitation of particles to isolate the difficulties associated with a flow environment. The purpose of this work; however, will focus on the software requirements to synchronize, collect and analyze light scattering patterns for a successful practical implementation.

1.3 Research Problem and the Objective

The theoretical perspective for the proposed research established is to primarily describe the diffraction of light theory commonly referred to as the Lorenz-Mie theory which is used to describe the far-field intensity pattern about the forward direction. This effect produced by the interaction of a laser beam with the light scattered by a known particle size is a complex formulation of the light scattering. Hence, a software simulation of the proposed theory integrates the angular properties of several particles of known sizes ranging from 5.12 μm to 19.5μm, and are used to set-up the framework for the experimental evaluations.

The research will use an acquisition system that is compatible for particle illumination by a laser beam. This system shall be described but the emphasis of this study will be governed by the interest and needs of developing a software interface. Also,

some synchronization mechanism will be required to collect the intensity signatures or scattering amplitudes. This interface will permit the off-line analysis of scattering patterns to be correlated with the theoretical approach.

This research topic has been approached and modeled in theory for static particles but with very few applications capable of being used to prove the theoretical approach in flow. Although there are many other ways of sizing particles, it may be useful to prove the feasibility of the well-defined theory in a flow environment.

The light scattering signatures from an illuminated particle is abundantly used in the flow cytometry area but are obtained from other means in capturing light information. The present study could determine the specific angles of interest allowing the discrimination by size of various types of particles. (e.g. blood cells)

1.4 Literature Survey

Different research groups have in recent years generalized the classic Lorenz-Mie theory to include non-plane waves. Of particular interest is the theory for the light scattered from a spherical particle placed in a Gaussian beam. This theory for the light scattered from a particle in a Gaussian beam is described by several authors [Borhen, 1983]. The Generalized Lorenz-Mie Theory (GLMT) introduces the light source to be considered as a non-plane wave and consequently taking place in the computation of the light scattering patterns [Gouesbet,1982]. The GLMT calculations will in theory give a complete description of the complex relations in a Phase Doppler Anemometer.

1.5 Research and Practical Objectives of this Thesis

Having provided this introduction as Chapter 1 of this thesis, Chapter 2 will present the theoretical presentation of the theory of light scattering of homogeneous, spherical and non-magnetic particles submitted to a plane wave incident beam. In addition, the case of the non-plane wave incident beam will be described as it fits the experimental data. Chapter 3 will describe the overall light scattering system with a strong emphasis on the imaging aspect. The sensor in use is introduced along with the frame grabber and the OLE control making up the imaging system.

Experimental results are described in Chapter 4 for determining the size of particles of interest from distribution profiles and using 2D-FFT of light scatter images. Some numerical examples are also given to show the effectiveness of the methods. Finally, the summary is drawn in chapter 5.

2 FUNDAMENTAL OF LIGHT SCATTER IMAGING

2.1 Maxwell Equations as a Foundation to Light Scatter

James Clerk Maxwell (1837-1879) gathered all prior knowledge in electromagnetics and described the whole theory of electromagnetics in four equations, called the Maxwell's equations.

These fundamental relations are considered laws of nature from which we can build the whole electromagnetic theory.

According to Helmholtz's theorem, an electrostatic model and a magnetostatic model are derived only by defining two fundamental vectors, the electric field intensity **E** and the magnetic flux density **B**,

An admissible electromagnetic field (E,H) must satisfy the vector wave equation described by the Maxwell's equation at all points where μ and ε are continuous. Using the complex representation of the electric (E) and magnetic induction (H) vectors, the Maxwell's equation assume the form

$$\nabla \bullet E = 0 \qquad (1)$$

$$\nabla \bullet H = 0 \qquad (2)$$

$$\nabla x E = i\omega\mu H \qquad (3)$$

$$\nabla x H = -i\omega\varepsilon E \qquad (4)$$

With ω the angular frequency, μ the permeability dependent of the medium under consideration but will be assumed to be independent of the fields, position and direction.

These key equations can be reformulated to establish the mathematical foundation of the light scatter phenomenon. What follows are two key aspects of such reformulation:

- To derive functions that relate to the Mie theory which will be described
- To consolidate the results of the Mie theory to light scatter.

2.1.1 Derivation of Key Functions to the Mie Theory

Defining,

$$k^2 \equiv \omega^2 \varepsilon \mu \qquad (5)$$

These key equations can be reformulated to establish the mathematical foundation of the light scatter phenomenon.

The Maxwell's equation may be written as :

$$\nabla^2 E + k^2 E = 0 \qquad (6)$$

$$\nabla^2 H + k^2 H = 0 \qquad (7)$$

Given a scalar function ψ and an arbitrary constant c, sometimes called the guiding or pilot vector, we may define a new vector M :

$$\mathbf{M} = \nabla x \, (\mathbf{c}\psi) \qquad (8)$$

If we use some vector identities, we can write:

$$\nabla^2 \psi + k^2 \psi = 0 \qquad (9)$$

if ψ is a solution of the scalar wave equation mentioned above, M satisfies the vector wave equation.

$$\nabla^2 M + k^2 M = 0 \qquad (10)$$

We may construct another vector **N** :

$$\mathbf{N} = (\nabla \times \mathbf{M})/k \qquad (11)$$

where it is also true that:

$$\nabla^2 \mathbf{N} + k^2 \mathbf{N} = 0 \qquad (12)$$

The problem of finding solutions to the field equations reduces to the simpler problem of finding solutions to the scalar wave equation. The scalar function ψ is called the generating function for the vector harmonics M and N

M and N become the solutions to the field equations where spherical symmetry is used. We choose functions ψ that satisfy the wave equation in the spherical polar coordinates r, θ, ϕ. A representation of these variables in terms of light scatter is shown in Figure 1.

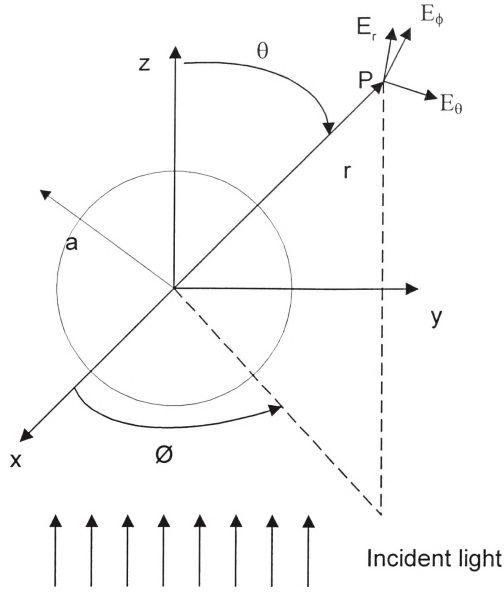

θ:scattering angle, ϕ:azimuthal angle

Figure 1. Illustration of the light scatter phenomena

As a pilot or guiding vector, we will choose r the radius vector so that M is a solution to the vector wave equation in spherical polar coordinates,

$$M = \nabla \times (r\psi) \qquad (13)$$

The scalar wave equation in spherical polar coordinates is:

$$\frac{1}{r^2} * \frac{\partial}{\partial r}\left(r^2 \frac{\partial \psi}{\partial r}\right) + \frac{1}{r^2.\sin\theta} \frac{\partial}{\partial \theta}\left(\sin\theta \frac{\partial \psi}{\partial \theta}\right) + \frac{1}{r^2.\sin\theta} \frac{\partial \psi^2}{\partial \phi^2} + k^2\psi = 0 \qquad (14)$$

The solution to equation (14) is of the form

$$\psi(r,\theta,\phi) = R(r)\,\Theta(\theta)\,\Phi(\phi) \qquad (15)$$

We can specify generating functions that specify the scalar wave equation in spherical polar coordinates.

$$\psi_{emn} = \cos(m\phi)P_n^m(\cos\theta)x_n(kr) \quad (16)$$

$$\psi_{omn} = \sin(m\phi)P_n^m(\cos\theta)x_n(kr) \quad (17)$$

where $x_n(r)$ is the spherical Bessel functions and $P_1^m(x)$ are the Legendre Polynomials.

The functions in equations (16) and (17) satisfying the scalar wave equation in the spherical polar coordinates may be expanded as an infinite series in:

$$\psi_{mn} = \sum_{i=0}^{\infty}\sum_{-1}^{1}[A_i^m \cos(m\phi)P_i^m(\cos\theta)x(kr)_n + B_i^m \sin(m\phi)P_i^m(\cos\theta)x(kr)_n] \quad (18)$$

2.1.2 Mie Theory, Amplitude Functions and Scattering Coefficients

The calculus becomes quite involved, so only the solution will be quoted here, see Borhen and Huffman for a detailed derivation. The infinite series in equation (18) does not solve the problem but rather show a mathematical coherence to be resolved by some change in the coordinate system. The boundary conditions are specified in spherical coordinates (in keeping with the symmetry of the particle), but the incident wave is planar and is still given in Cartesian coordinates.

In order to express the incident wave and boundary conditions in the same coordinate system, it is therefore necessary to either expand the plane wave in vector spherical harmonics, or the sphere boundary conditions in appropriate Cartesian coordinates. The conventional approach is to expand the plane wave in vector spherical

harmonics. The desired expansion of the complex plane wave in terms of spherical harmonics for the electric field E1 and the magnetic field H1 are given by equations (19) and (20).

$$E_1 = \sum_{n=1}^{\infty} i^n . E_0 \frac{2n+1}{n(n+1)} (c_n M_{o\ln}^{(1)} - i d_n N_{e\ln}^{(1)}) \qquad (19)$$

$$H_1 = -\frac{k_1}{w\varpi_1} \sum_{n=1}^{\infty} i^n . E_0 \frac{2n+1}{n(n+1)} (d_n M_{e\ln}^{(1)} + i c_n N_{o\ln}^{(1)}) \qquad (20)$$

Where μ_1 is the permeability of the sphere and k1 is the wave number in the sphere.

Through the use of asymptotic expression, the expansion of scattered field is :

$$E_s = \sum_{n=1}^{\infty} i^n . E_0 \frac{2n+1}{n(n+1)} (-b_n M_{o\ln} + i a_n N_{e\ln}) \qquad (21)$$

$$H_s = -\frac{k}{w\varpi} \sum_{n=1}^{\infty} i^n . E_0 \frac{2n+1}{n(n+1)} (a_n M_{e\ln} + i b_n N_{o\ln}) \qquad (22)$$

By defining supplementary functions $\pi_n(x)$ *and* $\tau_n(x)$, the E and H fields may be expressed in a reasonably concise form. The series of constants obtained are denoted a_n and b_n. Goody [Goody and Yung, 1989] gives these expressions, in slightly simplified form.

The amplitude functions S_1 and S_2 are the dimensionless complex scattered electric field amplitudes:

$$S_1(\theta) = \sum_{n=1}^{\infty} \frac{2n+1}{n(n+1)} [a_n \pi_n(\cos\theta) + b_n \tau_n(\cos\theta)] \qquad (23)$$

$$S_2(\theta) = \sum_{n=1}^{\infty} \frac{2n+1}{n(n+1)} [b_n \pi_n(\cos\theta) + a_n \tau_n(\cos\theta)] \qquad (24)$$

The scattering coefficients (a_n, b_n) are given as:

$$a_n = \frac{m.\psi_n(m.x).\psi'_n(x) - \psi_n(x).\psi'_n(m.x)}{m.\psi_n(m.x).\xi'_n(x) - \xi_n(x).\psi'_n(m.x)} \qquad (25)$$

$$b_n = \frac{\psi_n(m.x).\psi'_n(x) - m.\psi_n(x).\psi'_n(m.x)}{\psi_n(m.x).\xi'_n(x) - m.\xi_n(x).\psi'_n(m.x)} \qquad (26)$$

where m is the complex index of refraction of the particle with respect to its surrounding medium, x the size parameter described as

$$x = \pi.d/\lambda \qquad (27)$$

where λ is the wavelength illuminating the particle. The prime means the first derivative with respect to its argument located in parentheses.

The a_n and b_n scattering coefficients in (25) and (26) are not best suited for computations. These mathematical expressions may be formulated in a different fashion by introducing the logarithmic derivative given by (28):

$$D_n(\rho) = \frac{d \ln[\psi_n(\rho)]}{d\rho} \qquad (28)$$

$$a_n = \frac{[D_n(mx)/m + n/x].\psi_n(x) - \psi_{n-1}(x)}{[D_n(mx)/m + n/x].\xi_n(x) - \xi_{n-1}(x)} \qquad (29)$$

$$b_n = \frac{[m.D_n(mx) + n/x].\psi_n(x) - \psi_{n-1}(x)}{[m.D_n(mx) + n/x].\xi_n(x) - \xi_{n-1}(x)} \qquad (30)$$

where equations (29) and (30) were formed by using the following recurrence relations:

$$\psi_n'(x) = \psi_{n-1}(x) - n.\frac{\psi_n(x)}{x} \quad (31)$$

$$\xi_n'(x) = \xi_{n-1}(x) - n.\frac{\xi_n(x)}{x} \quad (32)$$

the logarithmic derivative satisfies the recurrence relation:

$$D_{n-1} = \frac{n}{\rho x} - \frac{1}{D_n + \frac{n}{\rho}} \quad (33)$$

$\psi_n(x)$ and $\xi_n(x)$ are the Riccati-Bessel functions defined as

$$\psi_n(x) = x j_n(x) \quad (34)$$

$$\xi_n(x) = x h_n^1(x) \quad (35)$$

These functions are related to the spherical Bessel functions $j_n(x)$ and $y_n(x)$ and the spherical Bessel functions of the third kind (or spherical Hankel functions $h^1{}_n(x)$ and $h^2{}_n(x)$ through the following:

$$j_n(\rho) = \sqrt{\frac{\pi}{2\rho}} J_{n+0.5}(\rho) \quad (36)$$

$$y_n(\rho) = \sqrt{\frac{\pi}{2\rho}} Y_{n+0.5}(\rho) \quad (37)$$

$$h_n^1(\rho) = j_n(\rho) + i y_n(\rho) \quad (38)$$

$$h_n^2(\rho) = j_n(\rho) - iy_n(\rho) \tag{39}$$

The angle-dependent functions π_n and τ_n defined as:

$$\pi_n(\cos\theta) = \frac{P_n^1(\cos\theta)}{\sin\theta} \tag{40}$$

$$\tau_n(\cos\theta) = \frac{dP_n^1(\cos\theta)}{d\theta} \tag{41}$$

The expressions S1 and S2 in equations (23) and (24) respectively contain functions π_n and τ_n which may be expressed in terms of the first and second derivative of the ordinary Legendre polynomials. It was first suggested by Hartel [Hartel, 1940] that the scattering functions could be simplified by the repeated use of recurrent relationships between the derivatives and products of the Legendre polynomials. For computation purposes, equations (40) and (41) may be expressed by upward recurrence:

$$\pi_n(\mu) = \frac{2n-1}{n-1}\mu.\pi_{n-1}(\mu) - \frac{n}{n-1}.\pi_{n-2}(\mu) \tag{42}$$

$$\tau_n(\mu) = n.\mu.\pi_n(\mu) - (n+1)\pi_{n-1}(\mu) \tag{43}$$

where $\mu=\cos(\theta)$ and starting with the initial coefficients needed for the recurrence to be defined $\pi_0=0$ and $\pi_1=1$.

A detailed account on the derivation of these functions is provided in Appendix A.

2.2 The Angle Dependent Scattering Functions

These functions as given in (40) and (41) take either positive or negative values. The lobes indicate positive values and absence of them indicate negative values. Polar

plots of π_n and τ_n are shown in Figure 2. The angles are ranging from 0 to 360 degrees. Additionally, we notice that as n increases, the number of lobes increases and the forward lobes becomes narrower.

For example, for n=3 and n=5

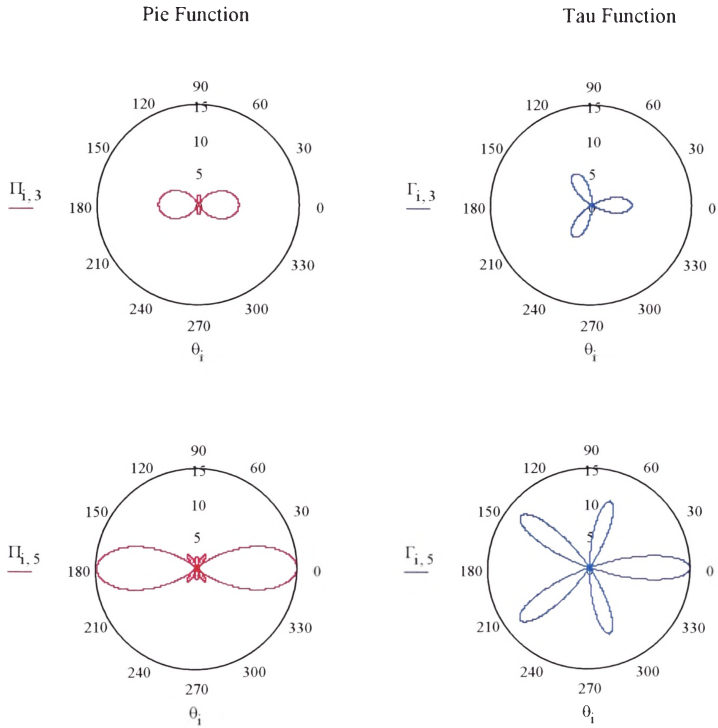

Figure 2. Polar Plot of the Angle Dependent Functions π_n and τ_n for n=3 and n=5

2.3 Simulation of the Mie Amplitude Functions

The equations (23) and (24) provided earlier are now simulated in terms of log of scattering intensity versus scattering angle in preparation for shedding light into the experimental setup about characterizing polystyrene particles.

The size of the particles have been selected to be 2.3, 4.2, 5.13, 8.0, 10.0, 15.0 and 19.5 μm. A detailed account on the derivation of these functions is provided in Appendix A. However, the collection of images of light scattering patterns were limited to 8, 15 and 19.5μm that corresponded to a stable and uniform experiment setup. Figure 3 denotes the two functions S1 and S2 and their representations for the Lorenz-Mie Theory.

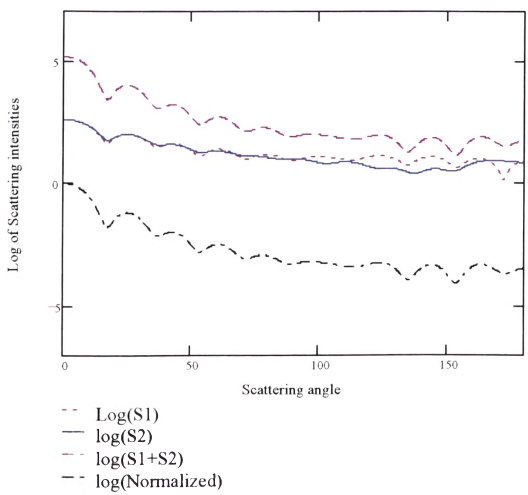

Figure 3. Log of Scattering Amplitudes S1, S2, S1+S2, and Normalized for a 2.3 μm particle

Other parameters and variables used to derive these scattering amplitude parameters are provided in Appendix B. In Figure 4, an illustration is given in terms of particle size for the case of 4.2, 5.13 and 8 μm particle.

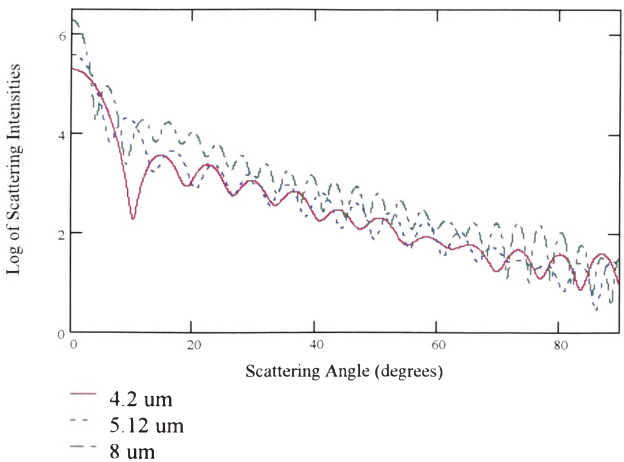

Figure 4. Scattering Amplitudes for a 4.2, 5.13, and 8 μm particle

In Figure 5, another illustration is given in terns of larger particles, namely 10, 15 and 19.5 μm.

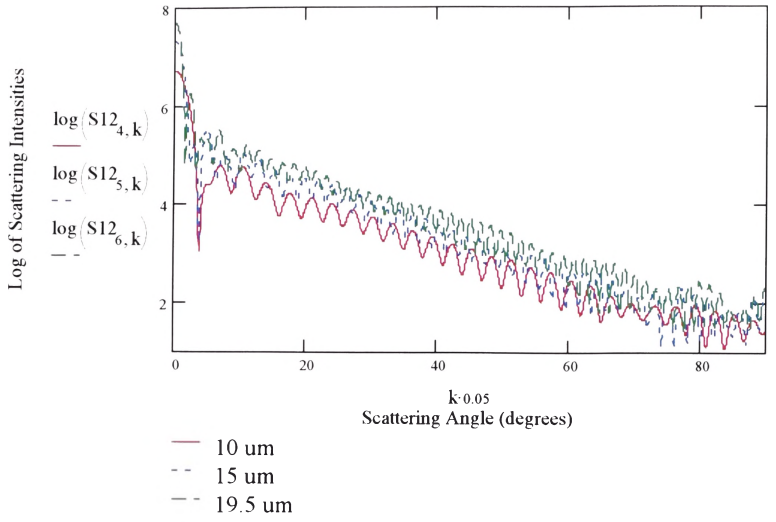

Figure 5. Log of Scattering Amplitudes for a 10, 15, and 19.5 μm particle

The log scale is used in Figure 3, 4, and 5 since the decaying rate on a linear scale would limit the graphical representation of the scattering amplitudes. Also, these amplitudes are represented with the log normalized for ease of comparison between particle sizes.

2.4 Generalized Theory of Scattering Particles for a Non Plane Incident Source Wave

2.4.1 Introduction

The main difference between the Lorenz-Mie theory and the Generalized Lorenz-Mie theory is the introduction of the g-factors. Different types of incoming waves correspond to different types of g-factors. The g-factors contain the information on the type of the incoming wave and the particle position in the wave. The g-factors can be calculated with the use of 3 different methods [Gouesbet, 1988]. As a general rule of

thumb it can be stated that GLMT and LMT gives the same results, when the diameter of the laser beam is bigger than the particle diameter and the particle is placed in the center of the laser beam. As illustrated in section 2.3, the Mie Theory interprets appropriately the scattering patterns for plane wave incident beams. However, this theory demands a specific input pattern. This input pattern must be characterized as a plane wave illuminating the particle. In this study and in most experiment on this topic, the input wave should not be considered as uniform as a plane wave light source but as a Gaussian beam (laser beam). It has been shown in the past [Gouesbet 93] that under specific requirements from the width of the laser beam can the effect of the source light be neglected.

Let's introduce the new scattering amplitudes S1 and S2 mentioned previously in (23) and (24) respectively, under a new criterion: the incident beam must be described. Taking into account the incident beam, namely the laser beam to interfere with the light scattering, uniquely involves the properties of the incident light and is independent of the properties of the particle. The scattering amplitudes have been modified and are defined by [Gouesbet, 1982]:

$$S_1(\theta) = \sum_{n=1}^{\infty} \frac{2n+1}{n(n+1)} \cdot g_n \cdot [a_n \pi_n(\cos\theta) + b_n \tau_n(\cos\theta)] \qquad (44)$$

$$S_2(\theta) = \sum_{n=1}^{\infty} \frac{2n+1}{n(n+1)} \cdot g_n \cdot [b_n \pi_n(\cos\theta) + a_n \tau_n(\cos\theta)] \qquad (45)$$

where g_n are called the Beam Scatter Coefficients (BSC) and describe the incident light. The scattering coefficients, a_n and b_n, and the Legendre functions, π_n and τ_n, described in equations (29), (30), (42), (43) respectively. The BSC are described as follows:

$$g_n = \frac{2n+1}{\pi^* n(n+1)} * \frac{1}{(-1)^n i^n} \int_0^{\pi} \int_0^{\infty} ikr \sin^2\theta . f . e^{-(ikr.\cos(\theta))} \psi_n^1(kr) P_n^1(\cos(\theta)) d\theta d(kr) \qquad (46)$$

where k is the wave number, the ψ_n^1 are the Bessel spherical functions and the P_n^1 are the associated Legendre Polynomials of order m =1. The function f is so called "the radial basic function" which describes all the information contained in the incident light. The BSC may be described using the following localized approximation [Gouesbet, 1988] of the Beam Shape Coefficients:

$$g_n = e^{[\frac{-(n+0.5)\lambda}{2\pi w_0}]^2} \qquad (47)$$

With w_0 representing the beam width. Assuming $w_{0 \to \infty}$, the laser beam approximates to a plane wave incident light. Consequently, for a large beam width compared to the particle diameter, g_n is then equal to 1 for all n and the scattering amplitudes become the ones established for the Lorenz-Mie Theory in equation (23) and (24).

It is of a great interest in this work to consider using the BSC (Beam Shape Coefficients) as a primary modification to the basic Mie theory. In chapter 3, we will address the concerns regarding the BSC and their impact on the experiment.

2.4.2 The Beam Shape Coefficients and their Impact on the Lorenz-Mie Theory

Let's show the effect of the Beam Shape Coefficients on the amplitude functions described for an arbitrarily chosen particle of d=4μm, a refractive index m=1.001 and a wavelength of λ=0.5145μm for both wo=5μm and wo=0.5μm. Figure 6 and Figure 7 only compare shape profiles. There is only a slight difference between the plane and non-plane input. However, the logarithmic scale used in Figure 6 tends to visually inhibit the difference. Figure 7 corresponds to w0=0.5μm and illustrates the case where the beam width is much smaller than the particle diameter. Furthermore, in this case the profiles greatly diverge from each other.

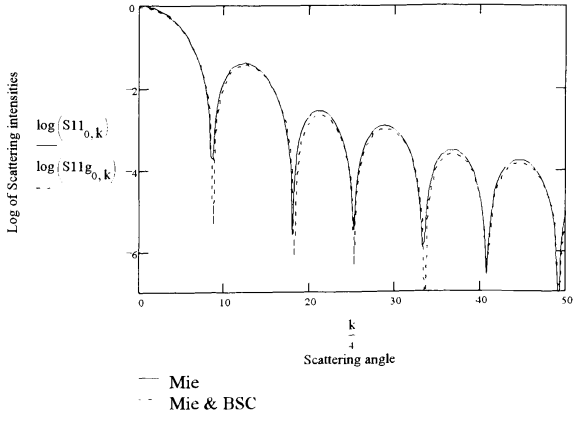

Figure 6. Comparison of LMT with LMT-BSC: m=1.001, λ=0.5145, d=4μm, w0=5μm

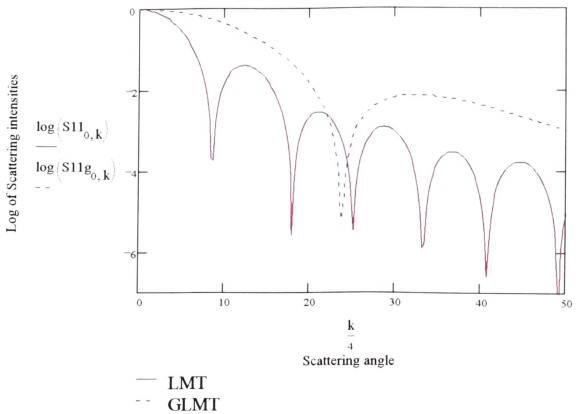

Figure 7. Comparison of LMT with LMT-BSC : m=1.001, λ=0.5145, d=4μm, w0=0.5μm

Let's demonstrate the impact of equation (47) with the particles that are of interest to us namely the one that will be used in our experiment. The following figures are considering one size particle with the Mie Theory and two different size of the incident light for the case of the Lorenz-Mie Theory including the BSC (LMT-BSC). Two values are selected, the first one close to the particle diameter and the other one half of the particle diameter.

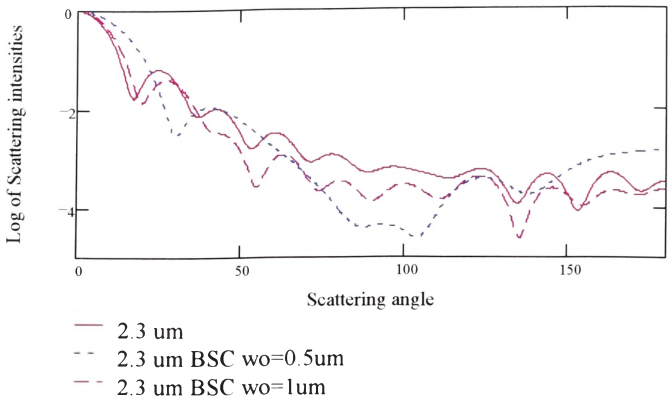

Figure 8. Comparison of LMT with LMT-BSC for 2 width of laser beam d=2.3μm

Let's show also for other particle size, the effect of using different beam size for the incident light. In Figure 9 , we illustrate the impact of using two different size of beam width, namely 1.25 μm and 2.5 μm. These 2 sizes represent a quarter and one half of the particle in consideration to illustrate the impact of the property of the light source with respect to the beam width.

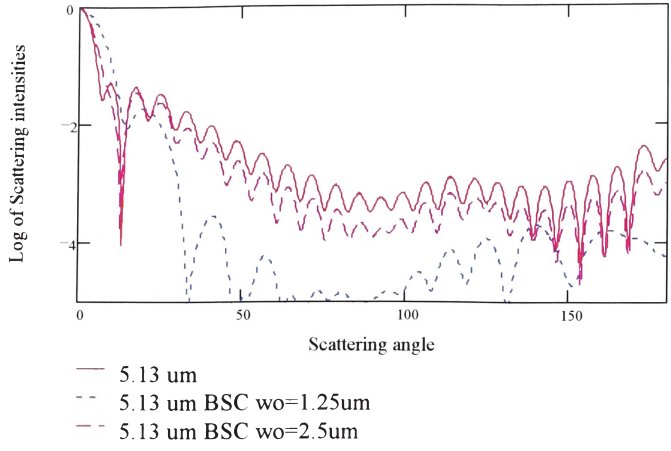

Figure 9. Comparison of LMT with LMT-BSC for 2 width of laser beam d=5.13μm

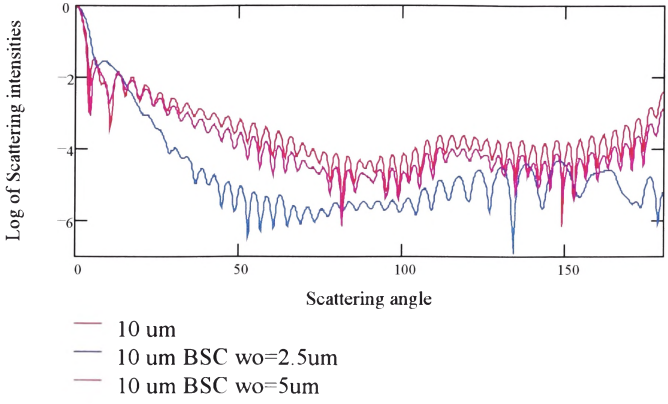

Figure 10. Comparison of LMT with LMT-BSC for 2 width of laser beam d=10μm

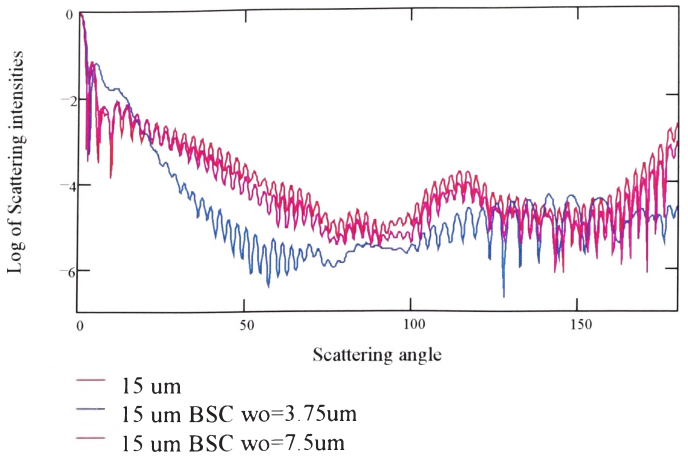

Figure 11. Comparison of LMT with LMT-BSC for 2 width of laser beam d=15 μm

Figures 8,9,10,11 are describing the effect of the beam width variation. The difference between plane wave scattering (Lorenz-Mie Theory) and the generalized theory taking into account the Beam Shape Coefficients increases when the particle increases relative to the beam radius. The width of the incident light must be considered carefully especially considering several particle being analyzed simultaneously and therefore choosing a beam width greater than the largest particle in use.

2.5 Parameters Sensitivity

The Lorenz-Mie theory is well suited for the theoretical analysis of homogeneous spherical particles illuminated by a plane source wave. However, the experiment in this thesis requires the use a non-plane wave source light, i.e. a laser. In addition to factor in

the Beam Shape Coefficients, other input parameters are required to calculate the scattering patterns such as particle diameter, complex refractive index and the wavelength of the input beam. The scattering patterns are directly related to these input and may affect considerably our ability to compare theoretical and experimental data.

Figure 12 shows the influence of a modification of the particle diameter. It appears that a small change in diameter of 0.1 μm significantly influences the patterns modifying both the angular location of the extrema and minima.

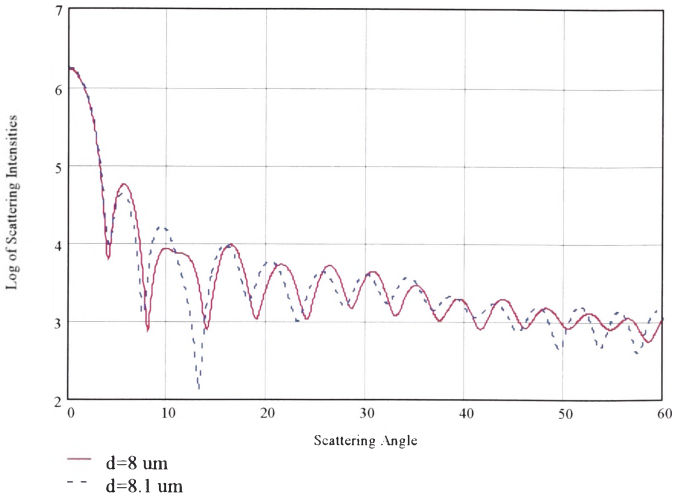

Figure 12. Sensitivity to the Particle Diameter.

The 0.1 μm diameter change in Figure 12 indicates a high sensitivity to the size of the particle. This change represents a 1.25% diameter error and may well characterize the manufacturer sensitivity to establish the standard deviation on the diameter of the particle.

3 Imaging Acquisition System

3.1 Light Scatter System

The system described here is based on a focused flow that uses DC as the triggering source along with a CCD camera for scatter image collection. The breadboard is a system for instrument control and image acquisition. The hardware includes a series of PC Board controllers, which receive instructions from a computer to drive solenoids and switches. The data acquisition is controlled by a PC Board. The DC output TTL pulse triggers the imaging system and transfers the scatter images from the CCD camera to the image acquisition board. An illustration of the system used in this thesis is shown in Figure 13.

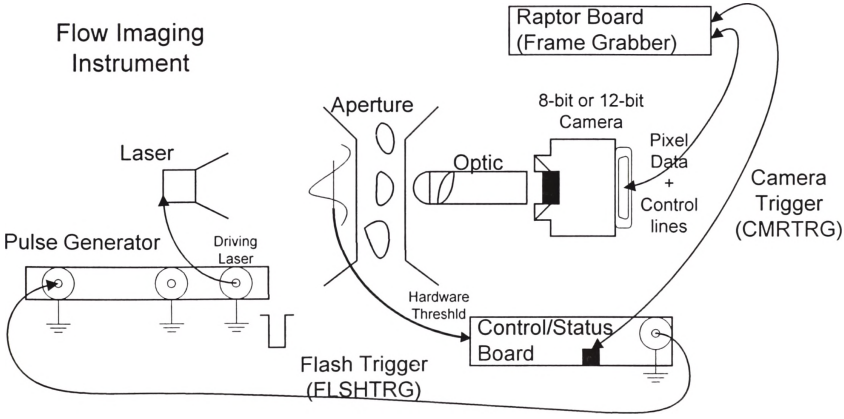

Figure 13. Flow Imaging Setup

This system consists of 4 main components, which are described briefly described below:

(1) Optics/Laser

(2) Frame Grabber / CCD

(3) Fluidics

(4) Electronics

1) The optical setup is made of optical and optoelectronic modules. The modules can be easily assembled and are connected with the aid of ring connectors.

   Laser: TOSHIBA (Model TOLD9150) 670 nm 15 mW diode laser
   Laser pulse electronics: Pulse generator
   Optics: Laser focusing lens (Newport PAC019 or PAC022)

2) CCD Camera:

   256x256x8bit, Model CA-D1-0256A (DALSA, Inc)
   Camera Configuration:
   Sensor IA-D1-0256, Pitch 16□m x16□m,
   Aperture 4.096mm x 4.096mm, Maximum Frame rate 220 fps.
   Frame Grabber: Raptor RAPPCIVS4 Image Frame Grabber Board

3) Fluidics
4) Data Acquisition System: Specification/description
   The data acquisition system consisted of a 150 Mhz PC running NT 4.0 with 64 MB memory. The system was configured with the following boards:
   National Instruments ATMIO16X data acquisition Board
   Raptor RAPPCIVS4 Image Frame Grabber Board

3.2 Practical Elements of the Image Capture Process

The experiments undertaken for the analysis of microscopic particles and their image capture were conditioned by the following practical considerations.

3.2.1 CCD Saturation Issue

A first consideration is the mask required limiting the beam waist into the sensor. Figure 14 illustrates the limitation of the image acquisition system.

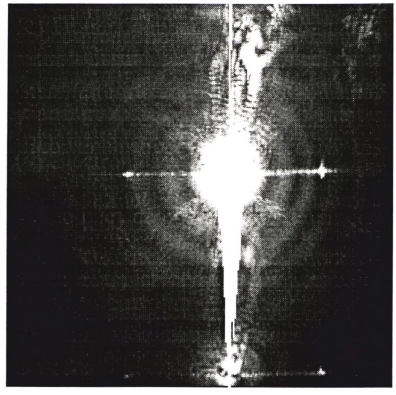

Figure 14. CCD bleeding. No Mask Blocking the Input Beam

The observation of scattering patterns is still possible but with an increase in pixel saturation known as blooming. The sensor in use, Dalsa IAD1-0256, does not have an anti-blooming mechanism designed to bleed off overflow from a saturated pixel. We have chosen an alternate method to reduce blooming by setting an opaque mask centered on the optical axis and in front of the sensor preventing the saturation of the central pixels. The addition of such a mask will avoid excessive bleeding as illustrated in Figure 14 but will introduce a loss of information at low angles.

Depending on the use of the imaging system, the mask may have a great or low impact on the analysis of light scattering patterns. In the case of a light scatter analysis driven by the interest of finding out the scattering information specific to scattering angles (i.e. intensity), the mask will prohibit the analysis of light scattering patterns for

which the mask is blocking such information. However, in this research thesis the goal is not to describe light scattering patterns for a specific angle but rather to obtain a specific characteristic (size) about the particle provoking the light scattering.

3.2.2 Image Acquisition Software Considerations

CCD → FrameGrabber → Object Linking and Embedding Display

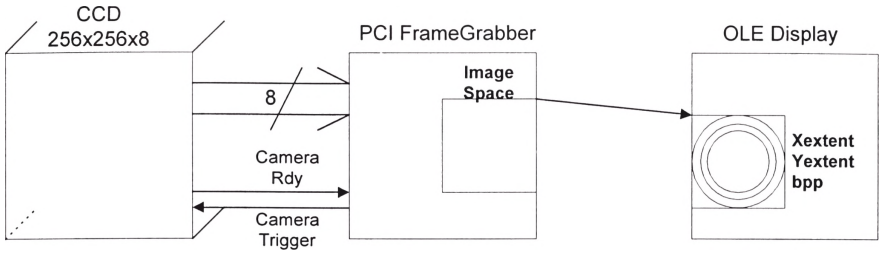

Figure 15. Image Transfer Process

3.2.2.1 CCD in Use

The CCD used in this system is a Dalsa sensor of 256x256 with 8 bit per pixel (bpp) resolution. The numbers of intensity levels are 2^8 or 256. Another camera, Dalsa 1024x1024x2^{12}, has been tested and considered to allow for the large dynamic range of scattering pattern intensities. This camera allows 4096 different pixel values, which is a considerable advantage over the smaller camera. Only later in the development of the real time interface that this camera was rejected because of a lack of responsiveness. The major drawback was actually the large size of the captured images: 2.09MB. Each pixel being expressed with 12 bit, its actual disk space only holding onto a 2-byte word, making it even less attractive.

3.2.2.2 Raptor (FrameGrabber)

A triggered, single frame, acquisition with the frame grabber (Raptor) and the digital camera is performed in the experiments. The camera has an asynchronous reset capability. Upon receipt of a trigger the Raptor will generate the reset pulse to the camera which will then dump its charge during the reset operation, expose a new frame and finally the Raptor will acquire the frame.

3.2.2.3 OLE in the Image Display

Object Linking and Embedding (OLE) is a technology that enables an application to create compound documents that contain information from a number of different sources. For example, a document in an OLE-enabled word processor can accept an embedded spreadsheet object. Unlike traditional "cut and paste" methods where the receiving application changes the format of the pasted information, embedded documents retain all their original properties. If the user decides to edit the embedded data, Windows activates the originating application and loads the embedded document.

In this research, such a tool is desired which allows reusability of the image display in the acquisition software and in an image-processing tool. As depicted in Figure 15, a real-time visualization software is required to display light scattering patterns as they are collected. An experiment may results in many captured images that requires a software structure to manage the large number of images collected at one time. This structured format is an “OLE structured storage”. This structure has been named “.IMG” and may contain many captured images in one single file. Figure 16 shows the basic structure of such storage.

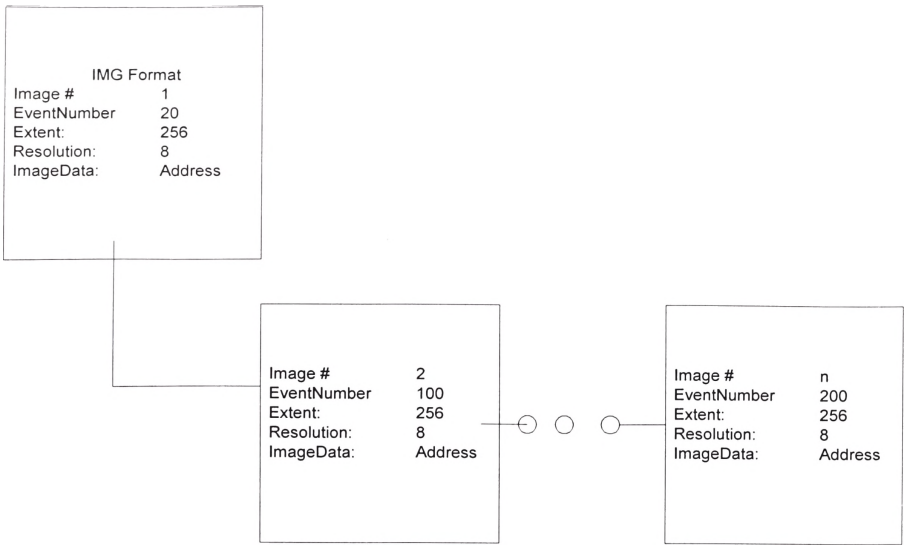

Figure 16. Image Collection Format

The OLE control contains a DIB (Device Independent Bitmap) that manages the actual pixel rendering. Once the DIB contains the pixels to display, the control allows manipulation of the pixels in various ways. A Region of Interest (ROI) has been implemented to facilitate the investigation of regions on the picture. A ROI is a zoomed view of a specific location of the image having a rectangular shape. This region is user-definable and its location and size are updated as the region is enlarged or reduced.

3.2.3 Flow Imaging Analysis Tool (FIAT)

This tool was developed to access efficiently the images of scattering pattern acquired through the imaging system. FIAT reads the .IMG format and displays all images belonging to one collection trough a user-friendly interface which incorporates the OLE control previously described in section 3.2.2.3. In addition to the visualization

aspect, the tool holds an extended range of common imaging filters such as pixel thresholding, logarithmic enhancement, high pass, low pass, image equalization, Laplacian, Sobel. Mappings are also available through the Polar and Logarithmic Polar transformation. Figure 17 illustrates the user interface of FIAT.

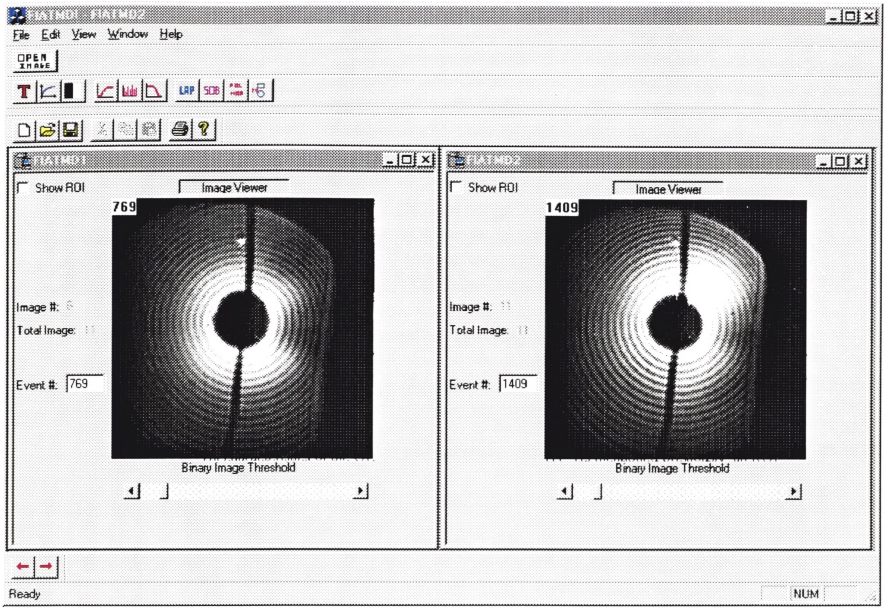

Figure 17. Flow Imaging Analysis Tool

All characteristics of the OLE control are exposed to FIAT. As mentioned previously, an ROI is available to the hosting software, which enables the zoom in capability with the option of saving this region into a .bmp image format. In the left of Figure 18 the ROI is visible and its zoomed-in region is illustrated in the right side of Figure 18.

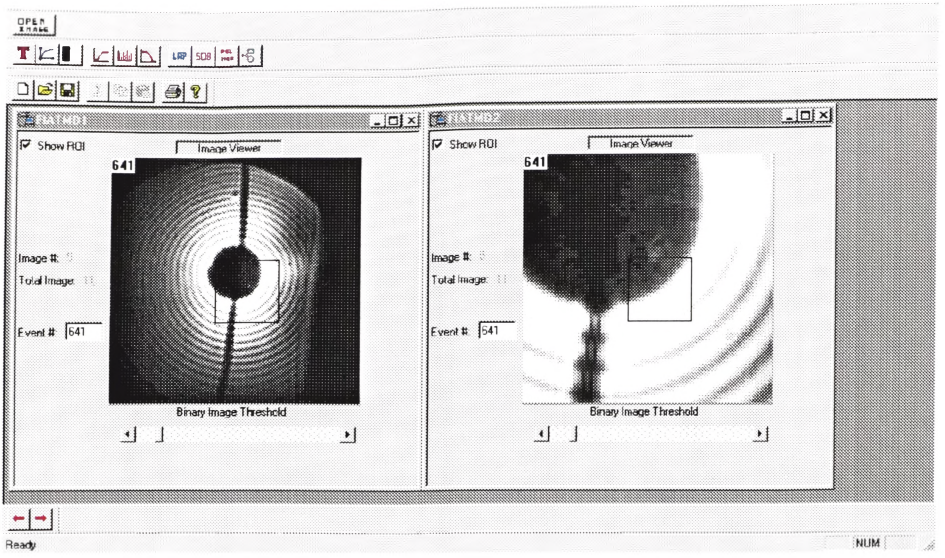

Figure 18. R.O.I/Zoom-in feature

3.2.4 Image Format Conversion Tool

Although the format created (IMG) retains many advantages with a large collection of light scattering patterns, it remains a non-standard image format. To account for this deficiency, a conversion tool was generated to ease the use of the light scattering pattern images outside of the FIAT environment. As shown in Figure 19, the images from a .img format may be selected individually or by a group of images to undergo the format conversion.

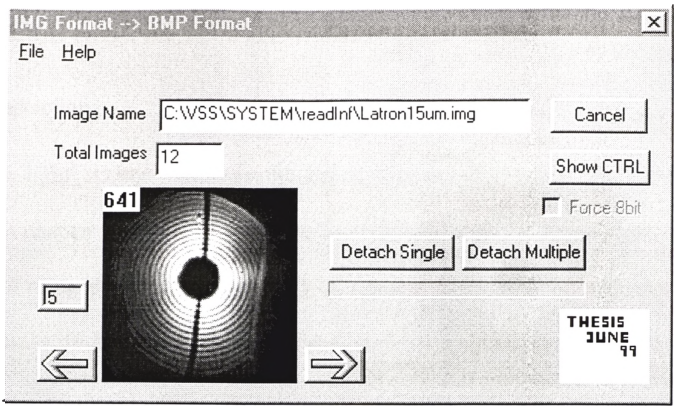

Figure 19. User Interface of Image Format Conversion Tool

A file or multiple files will be converted to a more standard format, namely BITMAP (.bmp) which is currently available in most image processing software or image analysis tools. These bmp files will be used in the next section to theoretically illustrate the Lorenz-Mie Theory that governs the light scattering patterns.

4 PARTICLE SIZING IN THE IMAGE CAPTURE

4.1 Introduction

The light scatter signatures modeled theoretically using the Lorenz-Mie as discussed in chapter 2 need at this stage to be correlated with the acquired signals through the practical setup described in chapter 3. A suitable analysis of the collected scattering patterns should provide a description of the particles responsible for the observed light scatter.

The first step deals with the confirmation of a valid correspondence between the observed and theoretical light scattering patterns. Using linear intensity distribution profiles, a mapping process can be established to generate intensity distribution profiles from a 2-D image signal, to 1-D intensity profiles as illustrated in Figure 20. The light scattering patterns uniquely described by the location of peaks and valleys associate the "rings" on the CCD array to the scattering angles.

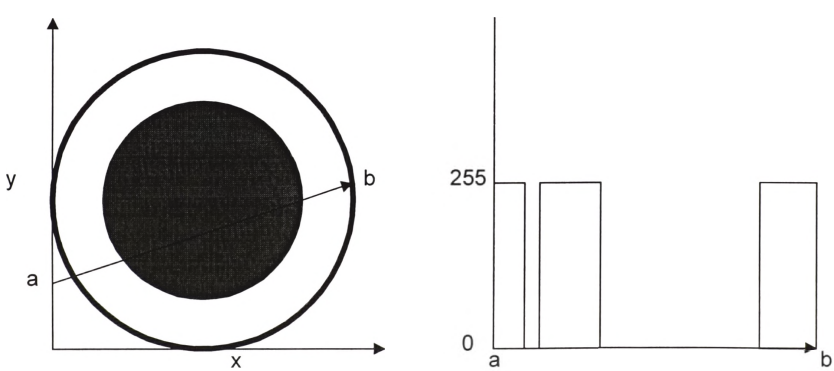

Figure 20. An Illustration of a Linear Intensity Distribution Mapping Between a 2-D Image and its corresponding 1-D Intensity Profile

The second step attempts to describe the scattering patterns from the 2-D scattering patterns containing frequency components that will in themselves characterize the scattering signatures back to the particle size.

In order to consolidate the above described data mappings with the Lorenz-Mie Theory, practical examples are assessed to determine the effectiveness of the intensity profiles collected on the CCD array. The following section confirms the relation between the light scatter rings of intensity and scattering angles required before establishing the proper technique to size the microscopic particles.

4.2 A Confirmation of the Collected Intensity Distribution Profiles with the Lorenz-Mie Theory

The purpose of this section is to determine the validity of the light scattering intensity profiles by associating the peaks and valleys created by the 1-D profiles to the ones obtained from the Lorenz-Mie theory simulation. Figure 21 recalls the modeled patterns from chapter 2 and illustrates their large intensity range between peaks. The large dynamic range of intensities precludes the observation of the complete signal, which oscillates throughout the scattering angle range.

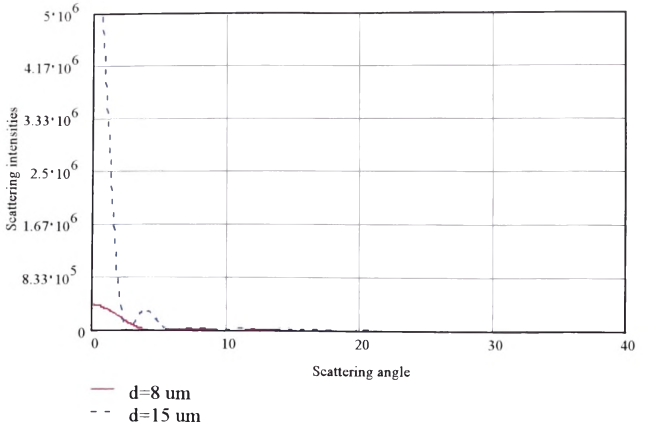

Figure 21. Linear Scale of Lorenz-Mie Theory for 8 and 15 μm particles.

Consequently, a better rendering of Figure 21 is obtained by omitting the first peak of each light scattering pattern. Figure 22 illustrates the intensity distributions in the vicinity of the second peak for particles of size 8 and 15 μm.

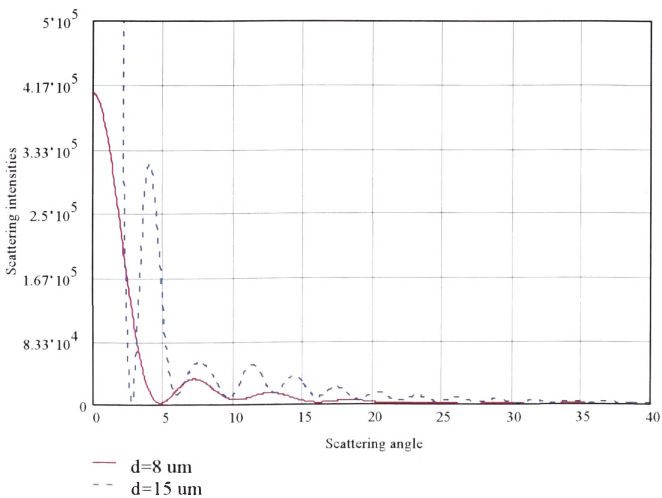

Figure 22. Change in Scaling of the Lorenz-Mie Theory of an 8 and 15 μm particle.

4.3 Diameter Estimation from Linear Distribution Profiles

The collected images on the CCD array are illustrated in Figure 23 (a) and (c) corresponding to particles of diameter 8 and 15 μm respectively. As mentioned in 3.2.1, an opaque mask centered on the optical axis and in front of the sensor prevents the saturation of the central pixels.

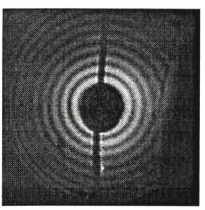

(a). D=8μm Particle

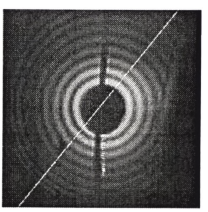

(b). D=8μm Particle + Line Profile

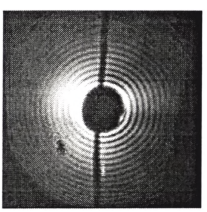

(c). D=15μm Particle

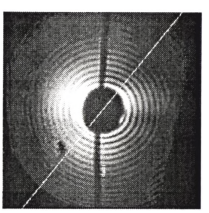

(d). D=15μm Particle + Line Profile

Figure 23. Scattering patterns and added line profile collected on the CCD array

A 1-D profile, as described in Figure 20, is obtained along the diagonal line to compute the intensity distribution profiles for particles illustrated in Figure 23 (b) and (d). This process is undertaken and the profiles are obtained in Figure 24 (a) and (b) for the 8μm particle and, (c) and (d) for the 15μm particle.

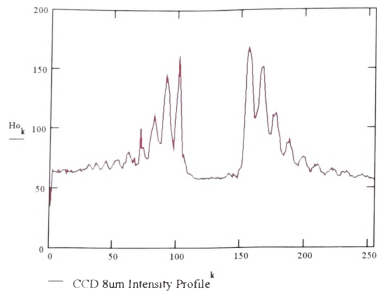

(a) Full ProfileD=8μm

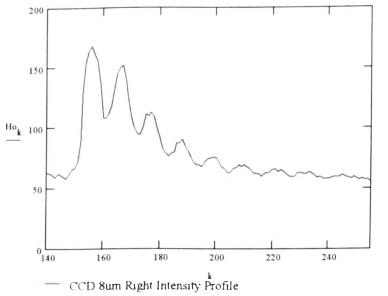

(b) Right ProfileD=8μm

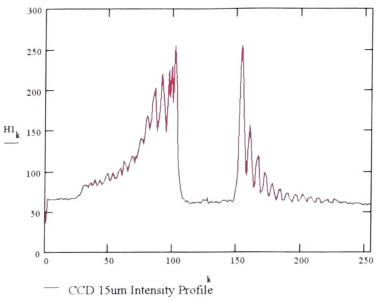

(c) Full ProfileD=15μm

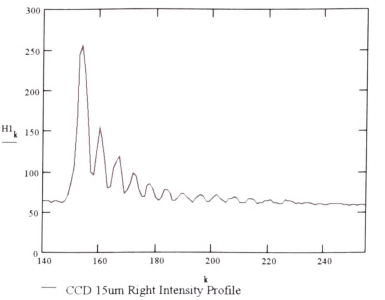

(d) Right Profile D=15μm

Figure 24. Linear Profiles of Scattering Patterns Observed on the CCD Array.

Let the distance between peaks and valleys in the light scatter linear profile be denoted by Δp_k and Δv_k, respectively. In order to calculate Δp_k and Δv_k, the location of peaks and valleys on the x-axis are computed and illustrated in Figure 25.

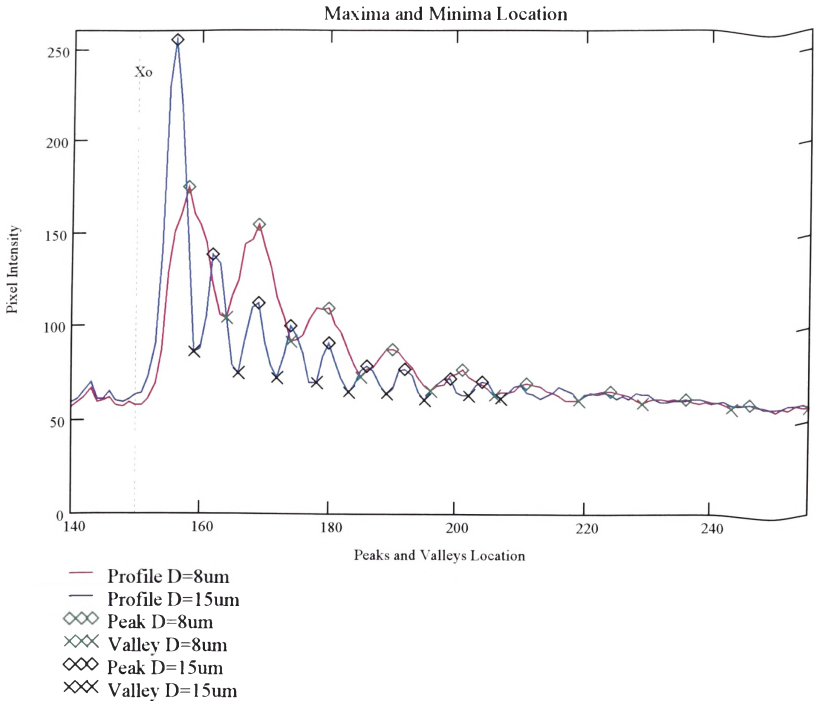

Figure 25. Localization of peaks and valleys for particles diameter 8μm and 15μm

Let's first prove that the line profiles are invariant to the ratio $\Delta p_k/\Delta v_k$. This ratio will remain unity as long as the collected light scattering patterns exhibit a constant distance between valleys and peaks. Equation 47 describes the concerned ratio PVR(Peak-to-Valley-Ratio):

$$PVR_i = \frac{\Delta p_i}{\Delta v_i} = \left(\frac{Xp_{i-1} - Xp_i}{Xv_{i-1} - Xv_i}\right), for \quad i = 0,1 \ldots n-1 \qquad (48)$$

where n is the number of peaks in the intensity profile. The results in applying equation 47 for particles of diameter 8μm and 15μm are illustrated in Figure 26.

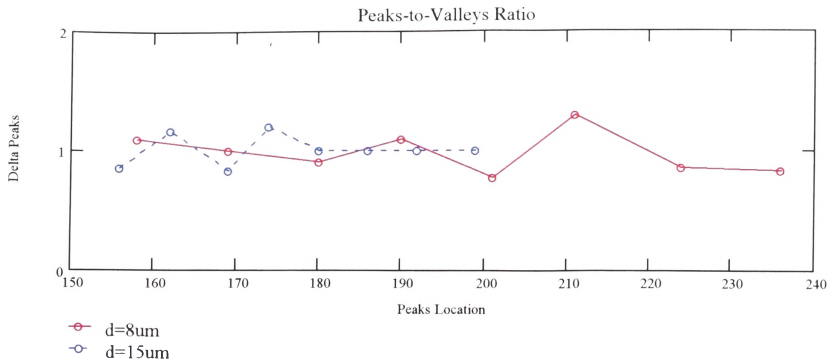

Figure 26. PVR for particles diameter 8μm and 15μm.

With these types of results established, let us define an actual (real world) measure of particle size as D_a and the calculated size of the particle as D_c. The following formulation are established to deduce the actual size of any given particle j under observation:

$$D_{c_j} = \left(\frac{1}{K \cdot \overline{\Delta p_{k_i}}}\right)_j, for\, j = 0..n-1 \qquad (49)$$

where K is defined as:

$$K = \frac{\sum_i k_i}{i} \qquad (50)$$

And where $\overline{\Delta p_{k_i}}$ is the average value of all Δp_{k_i} given by:

$$\overline{\Delta p_{k_i}} = \frac{1}{i} \cdot \sum \Delta p_{k_i} \qquad (51)$$

It is experimentally observed that the spacing between peaks Δp_k in the intensity profiles described in Figure 27 is inversely proportional to the size D_a of the particles under observation that is:

$$\overline{\Delta p_{kj}} \equiv \frac{1}{kDa} \qquad (52)$$

The number of peaks and valleys, necessary to establish a substantial calibration phase, is imposed by the size of the smaller particle in use. Referring back to Figure 23, a small particle exhibits wider and larger rings, Figure 23 (a), than would a large particle Figure 23 (c). Also, the distance between valleys (Δv_l) may as well be used to establish this calibration process. The distance between the peaks (Δp_k) is illustrated in Figure 27.

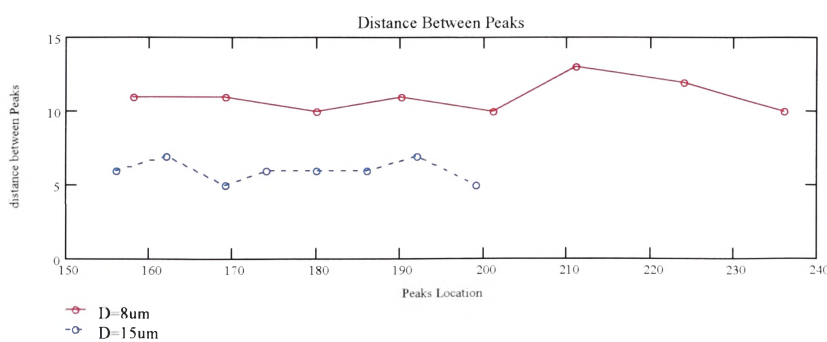

Figure 27. Δp_k (Distance between Peaks) for 8 and 15 μm Particles

We may now calculate k to establish the calibration step in order to estimate any particle size obtained from the same experiment set up. From equation (52), we deduce that:

$$k_i \equiv \frac{1}{\overline{\Delta p_{kj}} D_a} \qquad (53)$$

Considering the following two cases for D_a, the Δp_k and $\overline{\Delta p_{k\,i}}$ and k are given using the results previously shown in:

Case 1 for Da=8μm:

Δpk = [11 11 10 11 10 13 12 10]

$\overline{\Delta pk}$ =11

k_1=*0.0113636*

Case 2 for Da=15μm:

Δpk = [6 7 5 6 6 6 7 5]

$\overline{\Delta pk}$ =6

k_2=*0.01111*

The K constant finalizing the calibration step may be calculated from Equation 49:

$$\mathbf{K=0.011237373} \qquad (54)$$

We may now compute the calculated diameter for the two particles of diameter 8 and 15 μm using equation 48.

- 8μm particle:

$$Dc_8 = \left(\frac{1}{K.\overline{\Delta pk}}\right) = \mathbf{8.09}\mu m$$

- 15μm particle:

$$Dc_{15} = \left(\frac{1}{K.\overline{\Delta pk}}\right) = \mathbf{14.83}\mu m$$

The estimation of the error will be carried out in the next section, which will test and validate the calibration phase.

4.3.1 Testing of the Linear Intensity Profile Technique

Let's now demonstrate the use of the K parameter and apply it to a different particle size excluded from the calibration step. The particle in observation is selected to be of diameter 19.5 μm.

As previously described, a linear distribution profile is obtained for a particle of size 19.5 μm. The particle along with its linear profile are illustrated in Figure 28 (a) and Figure 28 (b) respectively.

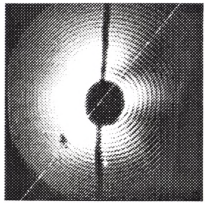

(a). D=19.5μm Particle Particle + Line Profile

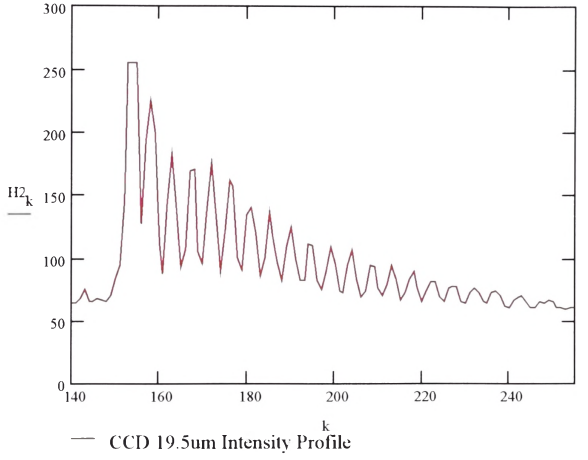

(b) Linear Intensity Profile for Testing

Figure 28. Test Particle and its Associated Linear Intensity Profile.

The distance between peaks Δp_k needs to be computed in the same fashion as for the calibration particles of 8 and 15 μm. Figure 29 illustrates the results of Δp_k for the particle in observation.

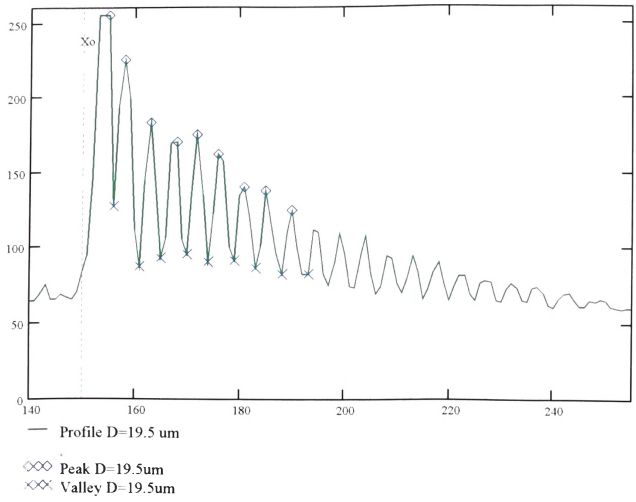

Figure 29. Localization of peaks and valleys for test particle of diameter 19.5μm

The test particle is then submitted to the calculation of its Δp_k, and the D_c is computed using the calibration constant K found in equation (53).

Test case for Da=19.5μm:
Δpk = [3 5 5 4 4 5 4 5]

$\overline{\Delta pk}$ =4.375

$$Dc_{19.5} = \left(\frac{1}{K.\overline{\Delta p_k}}\right) = 20.34\ \mu m \qquad (55)$$

4.3.2 Error Estimation for Size Determination from Linear Intensity Profile

The Estimated Error (ε), using percentages, is computed to evaluate the sensitivity of the system for the two particles used in the calibration step and for the particle used in the testing phase. The formula used to calculate ε is described in equation (56)

$$\varepsilon = \frac{|Dc - Expected\ Value|}{Expected\ Value} * 100 = \frac{|Dc - Da|}{Da} * 100 \qquad (56)$$

- Expected Value : 8 μm Dc_8=**8.09μm**

  ε_8= **1.125%**

- Expected Value : 15 μm Dc_{15}=**14.83μm**

  ε_{15}= **1.13%**

- Expected Value : 19.5 μm $Dc_{19.5}$=**20.34μm**

  $\varepsilon_{19.5}$= **1.7%**

4.4 Diameter Estimation Using the FFT of 2-D Light Scatter Images

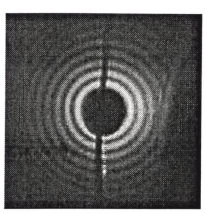

(a). 8μm Particle

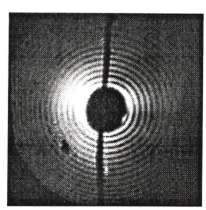

(b). 15μm Particle

Figure 30. 2-D Light Scatter Images

Figure 30 (a) and Figure 30 (b) are the illustrative images used to relate the light scattering patterns to their scattering angles. Ultimately, this relation will govern the calculation to estimate the diameter of the particles generating these scattering patterns.

From these 2 particles, one can notice that the distance between the peaks and valleys of the intensity magnitude profiles reveal a frequency pattern as earlier indicated in Figure 23 (a) and Figure 23 (c). A linear profile as shown in Figure 20 may describe these profiles which will generate 1-D patterns. However, the 2-D approach is undertaken to obtain frequency representations of the particles of size 8 and 15 μm. Furthermore, the

Fourier spectrum of these light scattering patterns reveals, through the principal frequency component, a direct proportionality to the size of the particle under observation.

These Fourier Domain representations are obtained through the use of 2-D Fast Fourier Transform (FFT) and are illustrated in Figure 31 (a) and Figure 31 (b).

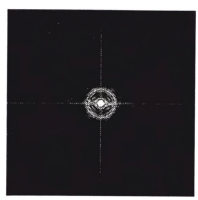

(a) FFT of 8μm Particle

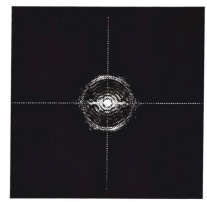

(b) FFT of 15μm Particle

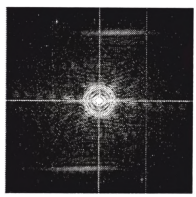

(c) Log Enhancement of (a)

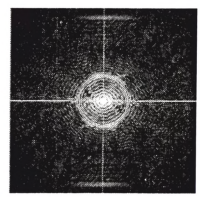

(d) Log Enhancement of (b)

Figure 31. FFT and its Logarithmic Enhancement

Each Fourier representation describes the frequency content of the light scattering signatures and reveals the highest frequency component by an outer circle. Figure 31 (c) and Figure 31 (d) emphasizes an outer circle due to an enhancing logarithmic scaling of the pixels intensity. This outer circle is the main frequency information describing the intervals of peaks and valleys in the image of the light scattering representation. In Figure

32 (a) and Figure 32 (b), we depict the location of this outer circle by increasing the grayscale intensity of all pixels belonging to this circle of diameter D_R.

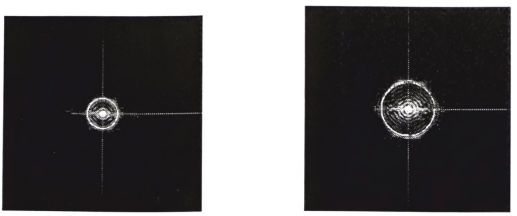

(a) 8μm **(b)** 15μm

Figure 32. Outer Ring Detection

The diameter of the outer ring (D_R) is now known and needs to be correlated with the actual particle size (D_a). The calculation are carried out in the frequency domain allows to deduct that the estimation of the diameter is directly proportional to the outer ring diameter:

$$D_a \equiv D_R * k \qquad (57)$$

where k is a constant to be determined. In a similar fashion, equation (53) is modified to accommodate for the domain change from spatial to frequency that is,

$$k \equiv \frac{D_a}{D_R} \qquad (58)$$

Using the two particles of size 8 and 15 μm, the diameter of the outer ring is used in calculating a constant K defined in equation (50).

Case 1 for Da=8μm:
$D_{R8} = 39$
$k_1 = 0.205$

Case 2 for D_a=15μm:
$D_{R15} = 66$
$k_2 = 0.227$

The K constant finalizing the calibration step may be calculated from Equation 47:

$$K=0.2162004662 \quad (59)$$

We may know compute the calculated diameter for the two particles of diameter 8 and 15 μm using equation (57).

- 8μm particle:
  $D_{c8} = K.D_{R8} =$ **8.432μm**

- 15μm particle:
  $Dc_{15} = K.DR_{15} =$ **14.269μm**

The estimation of the error will be carried out in the next section, which will again test and validate the calibration phase.

4.4.1 Testing of the FFT of 2-D Light Scatter Images

Let's now demonstrate the use of the K parameter and apply it to a different particle size excluded from the calibration step. The particle in observation is selected to be of diameter 19.5 μm and is described in Figure 33.

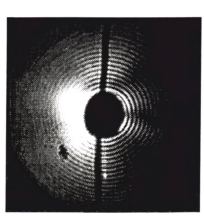

Figure 33. 2-D Light Scatter Images of a 19.5μm Particle

A Fourier Domain representation is obtained through the use of 2D Fast Fourier Transform (FFT) and its logarithmic enhancement are illustrated in Figure 34.

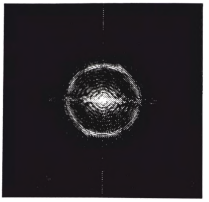

(a) FFT of 19.5 Particle

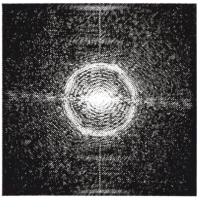

(b) Log Enhancement of (a)

Figure 34. FFT and its Logarithmic Enhancement for the test particle

The outer ring is detected and the located ring is illustrated in Figure 35.

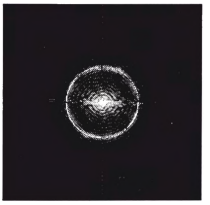

Figure 35. Outer Ring Detection

The test particle is then submitted to the calculation of its D_R and D_c is computed using the calibration constant K found in equation (59).

Test case for D_a19.5μm particle:

$DR_{19.5} = 92$

$D_{c19.5} = K.D_{R19.5} =$ **19.89**μm

4.4.2 Error Estimation for Size Determination from the FFT of 2-D Light Scatter Images

The Estimated Error (ε) is computed to evaluate the sensitivity of the system for the two particles used in the calibration step and for the particle used in the testing phase. The formula used to calculate ε is described in equation (56)

- Expected Value : 8 μm

  Dc_8=8.432μm

  ε_8= **5.4%**

- Expected Value : 15 μm

  Dc_{15}=14.269μm

  ε_{15}= **4.87%**

- Expected Value : 19.5 μm

  $Dc_{19.5}$=19.890μm

  $\varepsilon_{19.5}$= **2.00%**

More results are described in Table 1.

Actual Size / *Test Case*	*Da=8μm*	*Da=15μm*	*Da=19.5μm*
3	Dc_8 = 8.432μm ε_8= 5.40%	Dc_{15} = 15.134μm ε_{15}= 0.89%	$Dc_{19.5}$ = 19.458μm $\varepsilon_{19.5}$= 0.21%
4	Dc_8 = 8.432μm ε_8= 5.40%	Dc_{15} = 14.269μm ε_{15}= 4.87%	$Dc_{19.5}$ = 19.025μm $\varepsilon_{19.5}$= 2.43%
5	Dc_8 = 8.432μm ε_8= 5.40%	Dc_{15} = 14.269μm ε_{15}= 4.87%	$Dc_{19.5}$ = 19.674μm $\varepsilon_{19.5}$= 0.89%
6	Dc_8 = 8.432μm ε_8= 5.40%	Dc_{15} = 14.918μm ε_{15}= 0.55%	$Dc_{19.5}$ = 19.242μm $\varepsilon_{19.5}$= 1.32%

Actual Size / *Test Case*	*Da=8μm*	*Da=15μm*	*Da=19.5μm*
7	Dc_8 = 8.216μm ε_8= 2.69%	Dc_{15} = 15.134μm ε_{15}= 0.89%	$Dc_{19.5}$ = 19.242μm $\varepsilon_{19.5}$= 1.32%
8	Dc_8 = 8.432μm ε_8= 5.40%	Dc_{15} = 14.702μm ε_{15}= 1.99%	$Dc_{19.5}$ = 19.674μm $\varepsilon_{19.5}$= 0.89%
Averages	**Dc_8 = 8.396μm** **ε_8=4.94%**	**Dc_{15} = 14.737μm** **ε_{15}= 2.34%**	**$Dc_{19.5}$ = 19.39μm** **$\varepsilon_{19.5}$= 1.18%**

Table 1. Test Cases on Several Particles

Results in Table 1. are described in Appendix C.

5 CONCLUSION

A hardware-software integration of a light scattering system has been presented to relate the scattering patterns provoked by the illumination of a spherical particle to its size characteristic in a flow environment.

In order to achieve such a goal, key components have been developed and implemented.

A software interface allows the capture and display of real time captured images. This interface is based on an Object Linking and Embedded (OLE) architecture, which allows the reusability of this component into any software architecture supporting this environment. This structure is also the base of a visualization tool, rendering captured images and applying image filters and transforms as needed. In addition to image filters and transforms, a zooming capability is also available to scrutinize region of interests giving a flexible property to the understanding of the content of light scattering patterns.

In order to solve the inverse scattering problem, which determine particle properties from knowledge of the scattered fields, two approaches have been developed and implemented. The first approach deals with a linear distribution profile described in Chapter 4.3 which relates the light scattering patterns featuring an inverse proportionality to the particle size. The second approach uses the principal frequency component of the 2-D light scattering patterns by using its transform in the Fourier domain and is described in Chapter 4.4. The transformations to the Fourier domain are realized through the Fast Fourier Transform revealing a direct proportionality with the particle size. The high frequency component of this transform are retrieved and utilized to determine the particle size.

Both approaches are using algorithms based on observed data using an experimental set-up whose output (light scattering images) are consolidated by those outputs computed using the Lorenz-Mie Theory. Both theoretical and experimental results are recalled in Figure 36 (a) and Figure 36 (b), respectively.

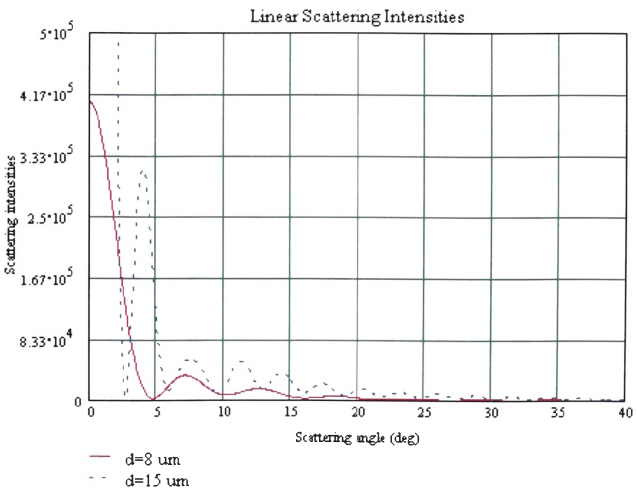

(a). Lorenz-Mie Theory

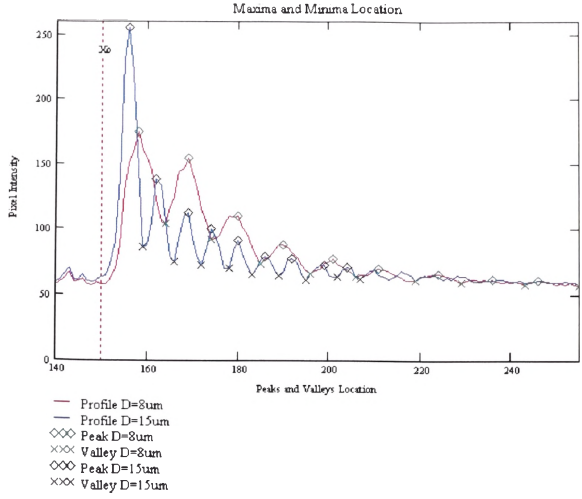

(b) Experimental Data

Figure 36. Light Scattering Patterns

Although both methods are satisfactory in terms of errors associated with the approximation of particle size, the second approach is preferred over the first one. The second approach is preferred because of its direct method bypassing the difficult task of determining a suitable line profile for the finding of peaks and valleys from the scattering intensity signature profiles.

LIST of REFERENCES

F. Corbin, G. Grehan, G. Gouesbet: *Top-Hat Beam Technique: Improvements And Application To Bubble Measurements,* Syst. Charact. 8 (1991) 222-228

Dave: *Coefficients Of The Legendre And Fourier Series For The Scattering Functions Of Spherical Particles*, Appl. Opt. 9, No. 8 (1970) 1888-1896

Goody, R. M. and Yung, Y. L. *Atmospheric Radiation: Theoretical Basis, 2nd ed.* New York: Oxford University Press, pp. 315-316, 1989.

G. Gouesbet, G. Grehan: *Sur La Generalisation De La Theorie De Lorenz-Mie,* Vol. 13, No2, pp.97-103 (1982)

G. Gouesbet, B. Maheu, G. Grehan: The Order Of Approximation In A Theory Of The Scattering Of A Gaussian Beam By A Mie Scatter Center, Opt. 16, No. 5 (1985) 239-247

G.Gouesbet, G. Grehan, B. Maheu.: Computations of the coefficients gn in the Generalized Lorenz-Mie theory using three different methods, Appl. Opt. 27 (1988) 4874-4884

G. Gouesbet, J. A. Lock, G. Grehan: Partial-Wave Representations Of Laser Beams For Use In Light-Scattering Calculations, Appl. Opt. 34, No.12 (1995) 2133-2143

G. Gouesbet: Generalized Lorenz-Mie Theory And Applications, Syst. Charact. 11 (1994) 22-34

G. Grehan, G. Gouesbet: Simultaneous Measurements Of Velocities And Sizes Of Particles In Flow Using A Combined System Incorporating A Top-Hat Beam Technique, Appl. Opt. 25, No. 19 (1986) 3527-3537

G. Grehan, B. Maheu, and G. Gouesbet: Scattering Of Laser Beams By Mie Scatter Centers: Numerical Results Using A Localized Approximation, Appl. Opt. 25 No. 19 (1986) 3539-3548

F. Guilloteau, G. Grehan, and G. Gouesbet: Optical Levitation Experiments To Assess The Validity Of The Generalized Lorenz-Mie Theory, Appl. Opt. 31, No. 15, (1992) 2942-2951 J.V.

W. Hartel, Das Licht 40, 141 (1940)

J.T. Hodges, G. Grehan, G. Gouesbet, and C. Presser: Forward Scattering Of A Gaussian Beam By A Nonabsorbing Sphere, Appl. Opt. 34, No.12 (1995) 2120-2132

D. Lebrun, S. Belaid, C. Ozkul, K. Fang Ren, G. Grehan: Enhancement Of Wire Diameter Measurements: Comparison Between Fraunhofer Diffraction And Lorenz-Mie Theory, Opt. Eng. 35(4) (1996) 946-950

J. A. Lock, E. A Hovenac: Diffraction Of A Gaussian Beam By A Spherical Obstacle, Am. J. Phys. 61 (8) (1993) 698-707

J. A. Lock and J. T. Hodges: Far-Field Scattering Of An Axisymmetric Laser Beam Of Arbitrary Profile By An On-Axis Spherical Particle, Appl. Opt. 35, No.21 (1996) 4283-4290

J. A. Lock, J. T. Hodges: Far-Field Scattering Of A Non-Gaussian Off-Axis Axisymmetric Laser Beam By A Spherical Particle, Appl. Opt. 35, No. 33 (1996) 6605-6616

J. A. Lock, J. T. Hodges, G. Gouesbet: Failure Of The Optical Theorem For Gaussian-Beam Scattering By A Spherical Particle, Opt. 12, No. 12 (1995) 2708-2715

M. Maeda and K. Hishida: Application Of Top-Hat Laser Beam To Particle Sizing In LDV System, Dept. Of Mechanical Engineering, Keio University Kohoku-Ku Yokohama, 223 Japan (1987)

Mie, Ann. Phys. 25. 377(1908)

APPENDICES

APPENDIX A

$i := 0..360$ $\quad n := 2..150$ $\quad \theta_i := i \cdot \frac{\pi}{180}$

Initialization of the first 2 terms $\Pi_{0,i} := 0$ $\quad \Pi_{1,i} := 1$

$\mu_i := \cos(\theta_i)$

The Π and Γ functions are angle-dependent

$$\Pi_{n,i} := \frac{(2 \cdot n - 1) \cdot \mu_i \cdot \Pi_{n-1,i}}{n - 1} - \frac{n \cdot \Pi_{n-2,i}}{(n-1)} \qquad \Gamma_{n,i} := n \cdot \mu_i \cdot \Pi_{n,i} - (n+1) \cdot \Pi_{n-1,i}$$

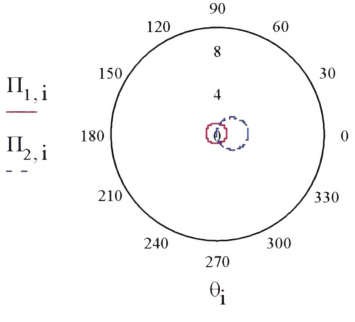

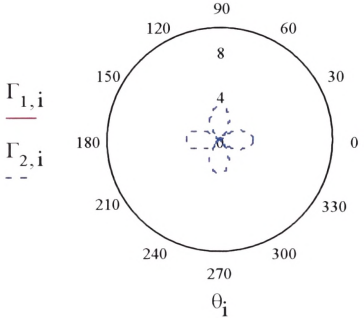

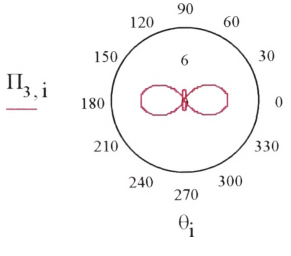

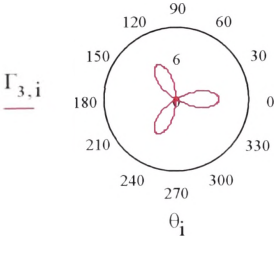

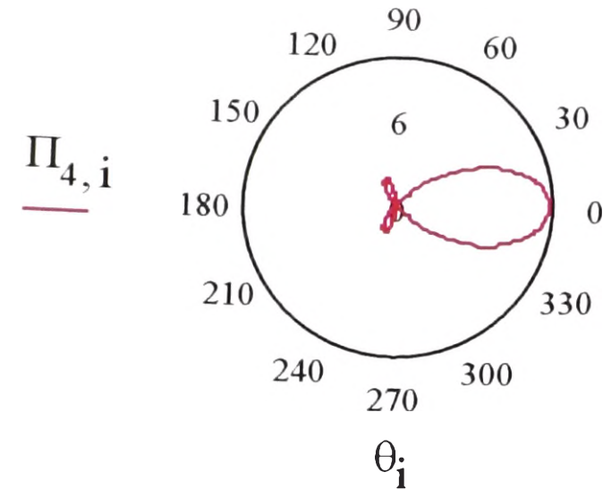
$\Pi_{4,i}$
90
120
60
150
6
30
180
0
210
330
240
300
270
θ_i

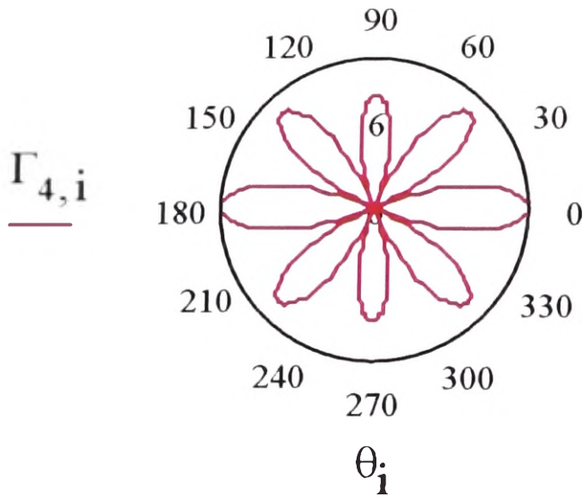
$\Gamma_{4,i}$
90
120
60
150
6
30
180
0
210
330
240
300
270
θ_i

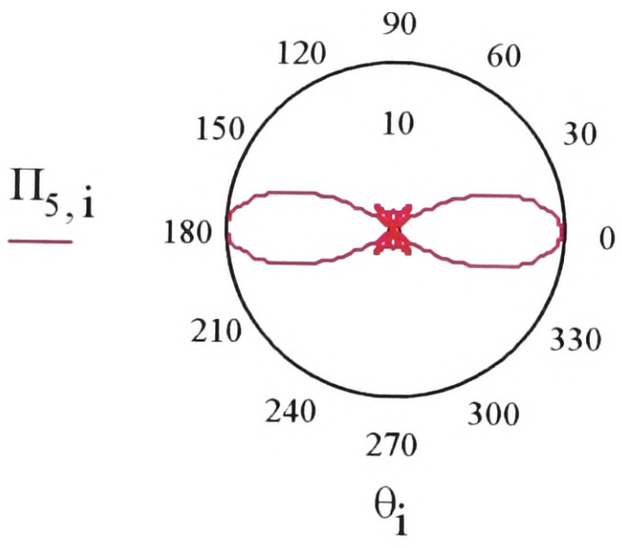
$\Pi_{5,i}$
90
120
60
150
10
30
180
0
210
330
240
300
270
θ_i

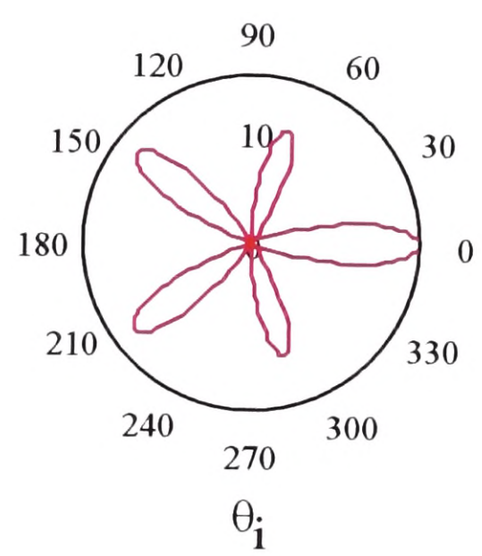
$\Gamma_{5,i}$
90
120
60
150
10
30
180
0
210
330
240
300
270
θ_i

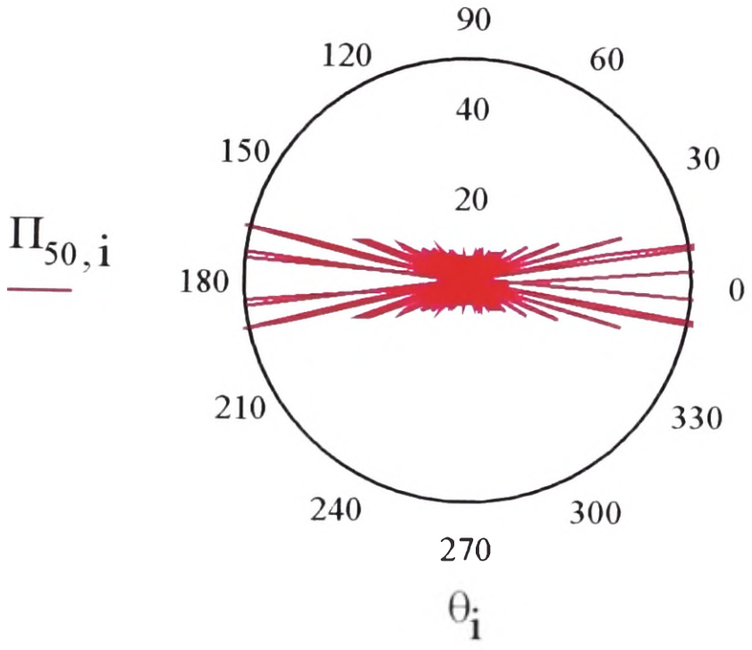
$\Pi_{50,i}$
90
120
60
40
150
30
20
180
0
210
330
240
300
270
θ_i

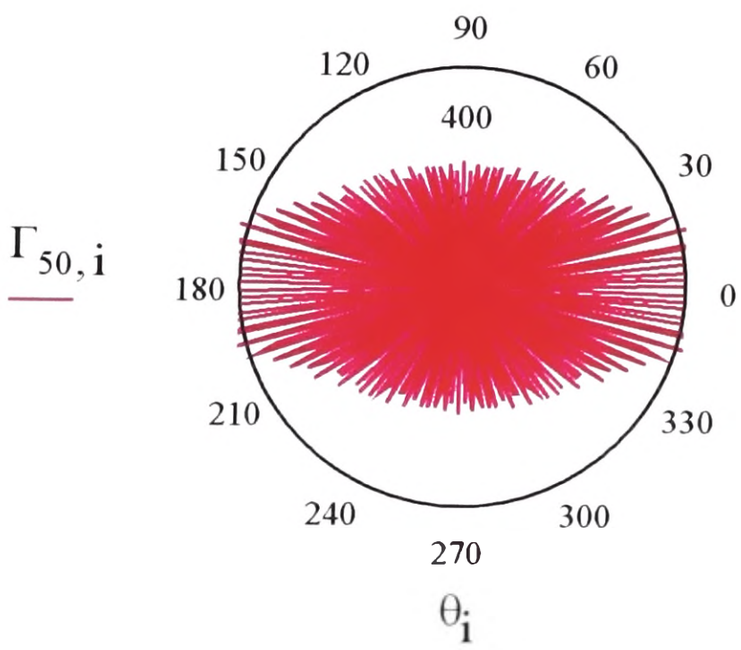
$\Gamma_{50,i}$
90
120
60
400
150
30
180
0
210
330
240
300
270
θ_i

APPENDIX B

The scattering coefficients may be simplified by using the Riccati-Bessel Function:

$\Psi_n(\rho) = \rho.J_n(\rho)$ Where J is the Bessel function

$\xi_n(\rho) = \rho.h_n(\rho)$ Where h is the spherical Hankel function

$k := 0 .. 1800$

$j := \sqrt{-1}$

$BeadDiameter_i :=$

2.3
4.2
5.13
8.0
10
15
19.5

Wave Number : $\lambda := 0.67$

$i := 0.. 6$ number of particles

Complex Refractive Index:

$$mm := \frac{1.58466564 + j \cdot 2.1466708210^{-6}}{1.3346}$$

$$radius_i := \frac{BeadDiameter_i}{2}$$

Size Parameter:

$$x_i := radius_i \cdot 2 \cdot \pi \cdot \frac{1}{\lambda}$$

$p := 0.. 300$

$n := 1.. 150$

$\rho_i := x_i \cdot mm$

$nn_p := 301 - p$

$q := 0.. 149$

Initial Values

$D_{i,301} := 0 + j \cdot 0$

$\psi_{i,0} := \sin(x_i)$

$\xi_{i,0} := \sin(x_i) - j \cdot \cos(x_i)$

$$\psi_{i,1} := \frac{\sin(x_i)}{x_i} - \cos(x_i)$$

$$\xi_{i,1} := \frac{\xi_{i,0}}{x_i} - (\cos(x_i) + j \cdot \sin(x_i))$$

$$\psi_{i,n+1} = \frac{2\cdot n+1}{x_i}\cdot\psi_{i,n} - \psi_{i,n-1}$$

$$\xi_{i,n+1} = \frac{2\cdot n+1}{x_i}\cdot\xi_{i,n} - \xi_{i,n-1}$$

Downward recurrence:

$$D_{i,nn_p-1} = \frac{nn_p}{\rho_i} - \frac{1}{D_{i,nn_p} + \frac{nn_p}{\rho_i}}$$

$$\tau_{q,k} = \Gamma_{k,(q+1)}\cdot\frac{2\cdot(q+1)+1}{(q+1)\cdot((q+1)+1)}$$

$$\pi_{q,k} = \Pi_{k,q+1}\cdot\frac{2\cdot(q+1)+1}{(q+1)\cdot((q+1)+1)}$$

$$A_{i,n} = \frac{\left(\frac{D_{i,n}}{mm} + \frac{n}{x_i}\right)\cdot\psi_{i,n} - \psi_{i,n-1}}{\left(\frac{D_{i,n}}{mm} + \frac{n}{x_i}\right)\cdot\xi_{i,n} - \xi_{i,n-1}}$$

$$B_{i,n} = \frac{\left(D_{i,n}\cdot mm + \frac{n}{x_i}\right)\cdot\psi_{i,n} - \psi_{i,n-1}}{\left(D_{i,n}\cdot mm + \frac{n}{x_i}\right)\cdot\xi_{i,n} - \xi_{i,n-1}}$$

$$a_{i,q} = A_{i,q+1}$$

$$b_{i,q} = B_{i,q+1}$$

$$S1 = a\cdot\pi + b\cdot\tau$$

$$S2 = a\cdot\tau + b\cdot\pi$$

$$S12_{i,k} = 0.5\left[\left(\left|S1_{i,k}\right|\right)^2 + \left(\left|S2_{i,k}\right|\right)^2\right]$$

$$SNor12_{i,k} = \frac{\left(\left|S1_{i,k}\right|\right)^2 + \left(\left|S2_{i,k}\right|\right)^2}{\left[\left(\left|S1_{i,0}\right|\right)^2 + \left(\left|S2_{i,0}\right|\right)^2\right]}$$

Amplitude Functions for particles size varying from 2.3 to 19.5μm

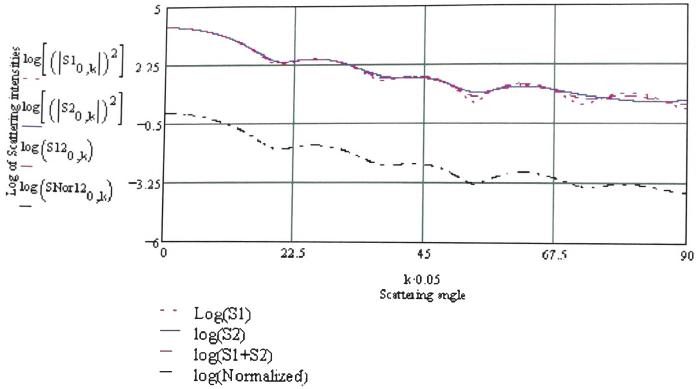

Figure 37. Particle D=2.3μm

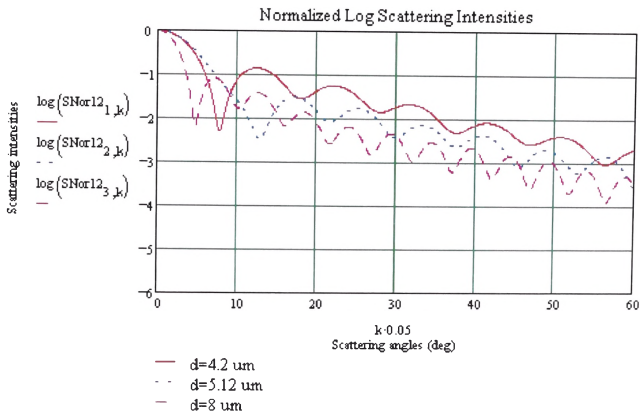

Figure 38. Particle D=4.2, 5.12, 8μm

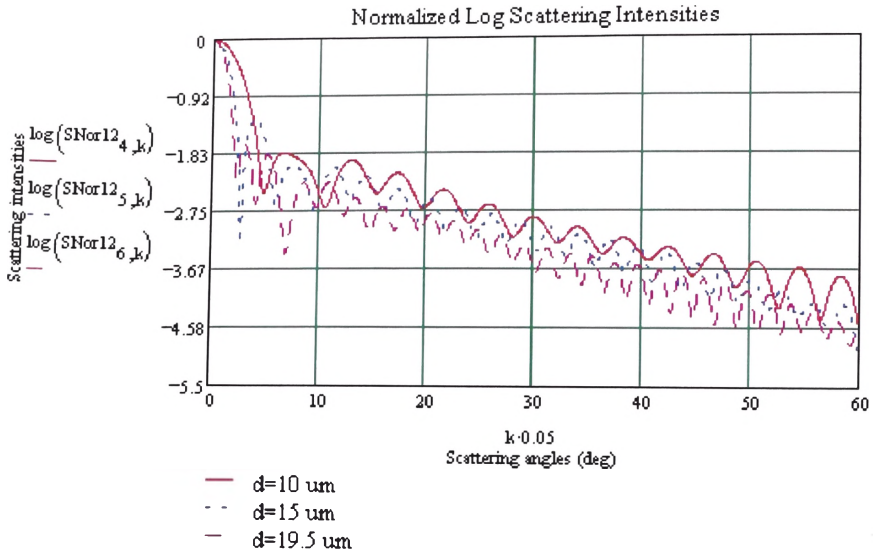

Figure 39. Particle D=10, 15, 19.5μm

APPENDIX C

The following illustrations are related to Table 1. The size estimation of the particles in interest are using the finding from :

$$K=0.2162004662 \quad (59)$$

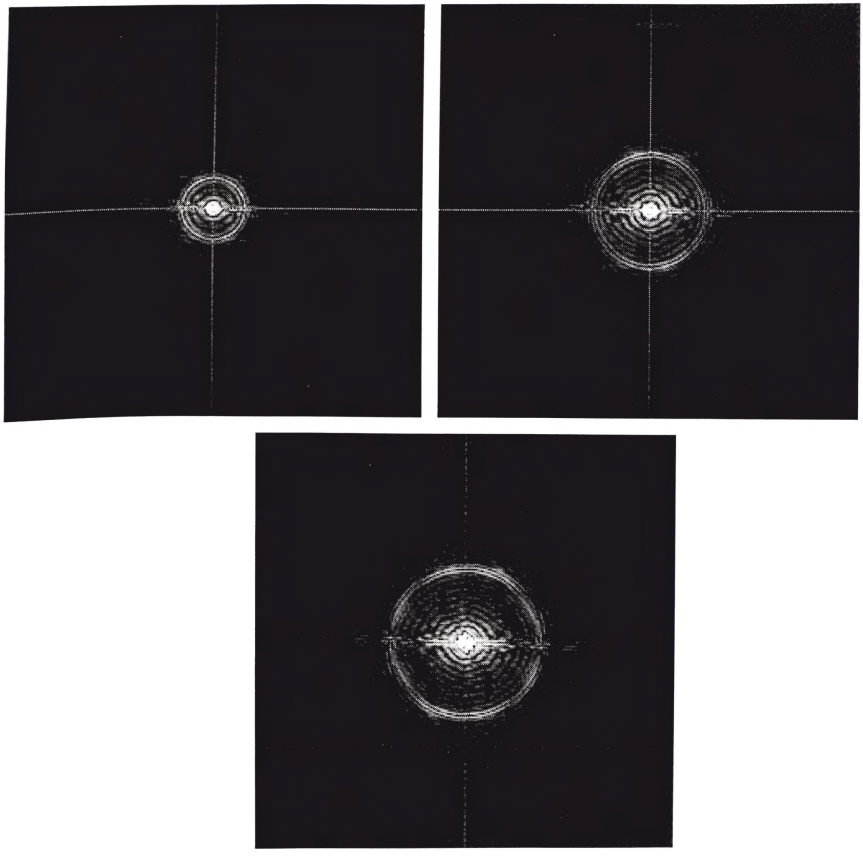

Figure 40. FFT Representation of 8, 15 and 19.5 um particles

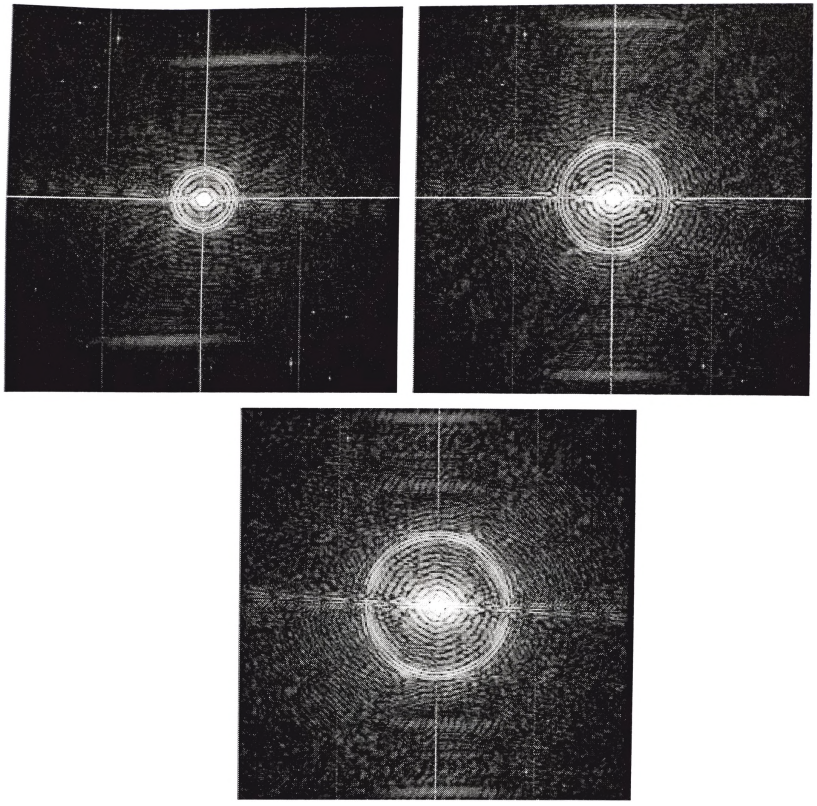

Figure 41. Logarithmic Enhancement of Figure 40

(ImgOut1 Integrate Diam8um) := FindOuterRing(Img1_1T_F2, M)
(ImgOut2 Integrate Diam15um) := FindOuterRing(Img2_1T_F2, M)
(ImgOut3 Integrate Diam19_5um) := FindOuterRing(Img3_1T_F2, M)
Calculated Diameter (Unitless)
Diam8um = 39
Diam15um = 66
Diam19_5um = 92
Proportional Constant :
kx=Particle Size/Computed Size

$$k1 := \frac{8}{Diam8um}$$

$$k2 := \frac{15}{Diam15um}$$

$$k3 := \frac{19.5}{Diam19\_5um}$$

k1 = 0.205

k2 = 0.227

k3 = 0.212

Averaged Constant:

$$K := \frac{k1 + k2}{2}$$

K = 0.2162004662

Size determination through K constant:

P8um := K·Diam8um

P15um := K·Diam15um

P19_5um := K·Diam19_5um

P8um = 8.432

P15um = 14.269

P19_5um = 19.8904

k1 = 0.205

k2 = 0.227

$$err8 := \frac{|P8um - 8|}{8} \cdot 100$$

err8 = 5.398

$$err15 := \frac{|P15um - 15|}{15} \cdot 100$$

err15 = 4.872

$$err195 := \frac{|P19\_5um - 19.5|}{19.5} \cdot 100$$

err195 = 2.002

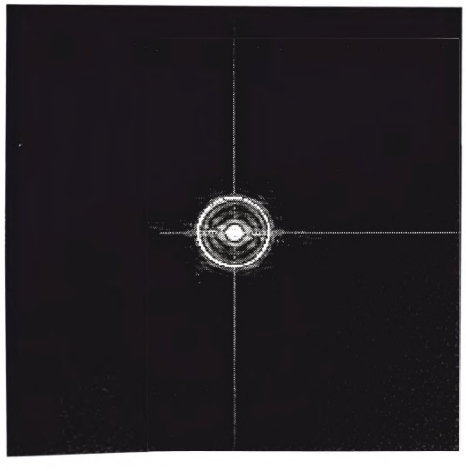

Figure 42. Outer Ring Localization for d=8μm

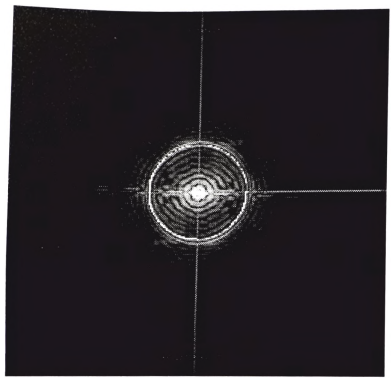

Figure 43. Outer Ring Localization for d=15μm

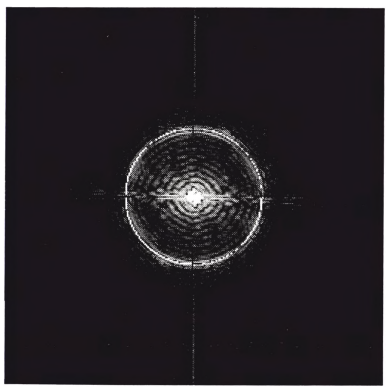

Figure 44. Outer Ring Localization for d=19.5μm